Photoionization and High Density Gas

T. Kallman & M. Bautista

Code 662, Lab. for High Energy Astrophysics, NASA/Goddard, Greenbelt, MD 20771

Received _____; accepted _____

ABSTRACT

We present results of calculations using the XSTAR version 2 computer code. This code is loosely based on the XSTAR v.1 code which has been available for public use for some time. However it represents an improvement and update in several major respects, including atomic data, code structure, user interface, and improved physical description of ionization/excitation. In particular, it now is applicable to high density situations in which significant excited atomic level populations are likely to occur. We describe the computational techniques and assumptions, and present sample runs with particular emphasis on high density situations.

Subject headings: X-rays: general – Ultraviolet: general

1. Introduction

Models for transport of radiation and the associated atomic processes have long divided into two broad categories: those applied to stellar atmospheres and those applied to nebulae. These distinctions originate from computational expediency and from the apparent distinction in nature between circumstellar and atmospheric gas. Efforts toward a unification of these two sets of assumptions are motivated by the realization that some of the gas which has been treated as nebular may actually have densities approaching that of traditional atmospheres, and from discoveries of the possible importance of external heating in atmospheres of, for example, X-ray binaries and accretion disks. In this paper we present models which are a partial step toward bridging the gap between nebular and atmospheric codes, along with some examples of applications which have not been previously accessible.

Traditional nebular modelling relies on several assumptions, including: neglect of excited atomic levels, except insofar as they mediate line emission; simple 2 stream and/or escape probability radiative transfer treatment; and steady-state ionization and thermal balance. The computational simplifications gained by these assumptions have allowed for the treatment of emission and absorption by a relatively large number of bound-bound and bound-free transitions in ions from the most astrophysically abundant elements, including both collisional and radiative processes. This has been extended from the optical and UV into both X-ray and IR wavelength bands, thereby encompassing ions ranging from neutral (including molecules) to fully stripped.

Stellar atmosphere models necessarily treat the microphysical processes affecting atomic level populations in sufficient detail to achieve LTE conditions in the proper limits. This, together with the solution to the radiative transfer equation, constrains the treatment of atomic processes more than for the nebular case. In spite of this, there have been many recent advances in the treatment of atomic processes in the context of stellar atmospheres,

made possible in large part by the accelerated lambda iteration methods for treatment of radiative transfer. As a result, atmospheric models are now capable of treating the atomic transitions involving thousands of levels in a full non-LTE calculation. These efforts have recently been reviewed by Hubeny (1998). However, there is still a disparity between the comprehensiveness of the atomic rates treated by atmospheric codes when compared with nebular codes, and this is most notable for processes affecting the X-ray spectral band.

In this paper we describe an attempt to improve the treatment of some aspects of the microphysics in nebular codes. This includes systematic treatment of radiative and collisional processes in such a way as to allow for an accurate convergence to LTE under suitable conditions, and also a comprehensive examination of the known rate constants describing such processes. In doing so, we have used as a point of departure the XSTAR v.1 code, which was originally presented in Kallman and McCray (1982), hereafter KM82. However, the present work represents a major revision in several areas. For this reason we attempt in what follows to describe the calculations in detail, in spite of the fact that this necessarily involves some repetition of the material presented in KM82. In the following sections we describe in turn, the computational method (Section II), some basic results which involve applications to problems similar to those discussed in KM82 (Section III), and summary and discussion (Section IV).

2. The Model

2.1. Assumptions

In this section we describe the computational procedure, assumptions, free parameters, and the quantities which are calculated. Chief among the assumptions is that each model consists of a spherical gas cloud with a point source of continuum radiation at the center.

Therefore it implicitly assumes spherical symmetry and radially beamed incident radiation. In principle, more complicated geometries can be mimicked by adding the local emission from various spherical sections with appropriately chosen conditions. Also important is the assumption that all physical processes affecting the state of the gas are in a steady-state, i.e. that the the timescales for variation in the gas density and illuminating radiation are long compared with timescales affecting all atomic processes and propagation of radiation within the gas. The validity of this assumption in any given situation depends on the conditions there, such as the gas density, temperature, and degree of ionization, and can be evaluated by using a model assuming steady-state and then calculating atomic rates which can (hopefully) justify the steady-state assumption a posteriori.

The primary difference between these models and atmospheric models lies in the treatment of the radiation field. In an optically thick atmosphere the state of the gas at any point in the cloud is coupled to the state of the gas in a large part of the rest of the cloud by the continuum radiation field and, in the limit of very large optical depth, can affect the excitation and ionization by suppressing radiative free-bound (recombination) transitions. We attempt to mimic some of these effects by assigning to each recombination event an escape probability, using an expression given in the following section. We also calculate the transfer of radiation by assuming that diffuse radiation emitted at each radius is directed radially outward or inward. These assumptions will be described in more detail later in this section.

A further assumption governs the treatment of the transport of radiation in spectral lines. Over a wide range of plausible situations large optical depths occur in the cores of lines of abundant ions, which may be important in cooling the gas. In treating the transfer of these photons we make the (conventional) assumption of complete redistribution in the scattering, which assumes that the transfer of the line photons occurs in a spatial region

very close to the point where the photons are emitted. Therefore the line emission rates are multiplied by an escape probability using an expression given in the following section. This factor is intended to simulate the line scattering in the immediate vicinity of the emission region, and it assumes that escape from this region occurs when the photon scatters into a frequency where the optical depth is less than unity. Following escape from the local region, the line photon is assumed to be subject to absorption by continuum processes which are treated using the same 2-stream transfer equation as for the continuum.

These assumptions are similar to some of those used in other calculations, and also differ in a few ways. Examples are the codes constructed by Ferland (Cloudy; cf. Ferland, 1996) and by Dumont, Collin and collaborators (Titan; Dumont, et al. (2000)). Many of the approximations made here with regard to the transfer of radiation are similar to those of Cloudy. Titan includes a treatment of Comptonization which makes it applicable to Thomson thick media and also a more accurate treatment of line transfer. Our treatment of the physical processes affecting excited levels is likely more detailed than those of these other calculations, particularly for elements with Z 2.

2.2. Input

The input parameters are the source spectrum, the gas composition, and the gas density or pressure. The spectrum of the central source of radiation is described by the spectral luminosity, $L_{0\varepsilon} = Lf_\varepsilon$, where L is the total luminosity (in erg s^{-1}). The spectral function, f_ε, is normalized such that $\int_0^\infty f_\varepsilon d\varepsilon = 1$ and may be of one of a variety of types, including: Thermal bremsstrahlung, $f_\varepsilon \sim \exp(-\varepsilon/kT)$; blackbody, $f_\varepsilon \sim \varepsilon^3/[\exp(\varepsilon/kT) - 1]$; or power law, $f_\varepsilon \sim \varepsilon^\alpha$; or the user may define the form of the ionizing continuum by providing a table of energies and fluxes. The gas consists of the elements H, He, C, N, O, Ne, Mg, Si, S, Ar, Ca, Fe, and Ni with relative abundances specified by the user. The

default abundances are the solar values given by Grevesse, Noels and Sauval (1996).

2.3. Elementary Considerations

When the gas is optically thin, the radiation field at each radius is determined simply by geometrical dilution of the given source spectrum f_ϵ. Then, as shown by Tarter, Tucker and Salpeter (1969), the state of the gas depends only on the ionization parameter $\xi = L/nR^2$, where L is the (energy) luminosity of the incident radiation integrated from 1 to 1000 Ry, n is the gas density, and R is the distance from the radiation source. This scaling law allows the results of one model calculation to be applied to a wide variety of situations. For a given choice of spectral shape this parameter is proportional to the various other customary ionization parameter definitions, i.e. $U_H = F_H/n$ (Davidson and Netzer (1979)), where F_H is the incident photon number flux above 1 Ry; $\Gamma = F_\nu(\nu_L)/(2hcn)$, where $F_\nu(\nu_L)$ is incident (energy) flux at 1 Ry; and $\Xi = L/(4\pi R^2 cnkT)$ (e.g. Krolik, McKee and Tarter (1981)).

In the optically thick case, Hatchett, Buff and McCray (1976), and Kallman (1984) showed that the state of the gas could be parameterized in terms of an additional parameter which is a function of the product of L and either n (the number density) or P (the pressure), depending on which quantity is held fixed. In the case n = constant, this second parameter is simply $(Ln)^{1/2}$ (McCray, Wright and Hatchett (1977)). This parameter does not allow easy scaling of model results from value of Ln to another, since the dependence on this parameter is non-linear, but it does provide a useful indicator of which combinations of parameter values are likely to yield similar results and vice versa.

When the electron scattering optical depth, τ_e, of the cloud becomes significant, the outward-only approximation used here breaks down, and different methods of describing the

radiative transfer must be used (e.g. Ross (1979)). Therefore, the range of validity of the models presented here is restricted to $\tau_e \leq 0.3$, or electron column densities $\leq 10^{24}$ cm^{-2}.

2.4. Algorithm

The construction of a model consists of the simultaneous determination of the state of the gas and the radiation field as a function of distance from the source.

2.4.1. Atomic Level Populations

The state of the gas is defined by its temperature and by the ionic level populations. As a practical matter, we maintain the distinction between the total abundance of a given ion relative to its parent element (the ion fraction or fractional abundance) and the relative populations of the various bound levels of that ion (level populations), although such distinctions are somewhat arbitrary given the presence of transitions linking non-adjacent ion stages and excited levels of adjacent ions.

Calculation of level populations proceeds in 2 steps. First, a calculation of ion fractions is performed using total ionization and recombination rates into and out of each ion analogous to those used in XSTAR v.1 (KM82). Then we eliminate ions with abundance less than a fixed fraction ϵ relative to hydrogen from further consideration. Experimentation has shown that $\epsilon = 10^{-8}$ yields gas temperatures within 1% of those calculated using a larger set of ions for most situations when the density is low. This criterion leads to ion sets which can include up to 10 stages for heavy elements such as iron and nickel. We also make sure that the selected ions are all adjacent. i.e. we force the inclusion of ions which fall below our threshold if they are bracketed by ions which satisfy the abundance crterion.

The second step consists of solving the full kinetic equation matrix linking the various levels of the ions selected in step 1. We include all processes in the database which link the bound levels of any ion in our selected set with any other level, and also including the bare nucleus as the continuum level for the hydrogenic ion, if indicated. This results in a matrix with dimensionality which may be as large as 900. The equations may be written schematically as (*rate in*) = (*rate out*) for each level. In place of the equation for the ground level of the most abundant ion we solve the number conservation constraint.

We include collisional and radiative bound-bound transitions (with continuum photoexcitation), collisional ionization, photoionization, electron-ion recombination and 3-body recombination for all the levels of every ion for which the required atomic rate data is available. The effects of line scattering in all transitions are accounted for by taking into account the fact that line scattering reduces the net decay rate by repeated absorption and reemission of the line photon. An analogous procedure is used for free-bound (recombination) transitions.

2.4.2. Atomic Levels

A large fraction of recombinations occur following cascades from a very large number of levels close to the continuum. Since explicit treatment of these levels is not feasible, we treat this process as follows (this procedure, along with detailed descriptions of other aspects of the database and the multilevel scheme are described in detail in Bautista and Kallman (2000a)): For every ion we choose a set of spectroscopic levels starting with the ground level, which are responsible for the identifiable emission lines and recombination continua; there are typically 10 – 50 of these for most ions, although for a few ions we include $\geq$100 such levels. In addition we include one or more superlevels and continuum levels. The continuum levels represent bound levels of more highly ionized species (in

practice at most only a few such levels are of importance).

The superlevel is an artificial level used to account for recombination onto the infinite series of levels that lie above the spectroscopic levels. In H and He-like ions the superlevels also account for the recombination cascades of these high lying levels onto the spectroscopic levels, and the rates for such decays are calculated by fitting to the results of population kinetic calculations for individual ions which explicitly include $\geq$1000 levels. For these isoelectronic sequences we explicitly include excited levels with a spectator electron, which give rise to satellite lines. Excitation, radiative deexcitation, and electron trapping involving these levels accounts for excitation-autoionization, recombination, and radiation damping processes.

For other iso-electronic sequences full kinetic calculations are not yet available. For these ions the superlevels are assumed to decay directly to the ion's ground level, and the rates into and out of the superlevel are calculated in order to fit to the total recombination rates for the various ions (Bautista and Kallman (2000a), Bautista and Kallman (2000b)). This approach allows us to simultaneously account for the contributions of excitation, ionization, and recombination to the ion's level populations. In this way we solve ionization and excitation balance without the use of total recombination rates which is customary in many nebular calculations.

By using the approach described above and providing that every transition process accompanied by its detailed balance inverse process we insure that the level populations will naturally converge to LTE under proper conditions.

2.4.3. Thermal Equilibrium

The temperature is found by solving the equation of thermal equilibrium, which may be written schematically as $(Heating) = (Cooling)$. This is solved simultaneously with the condition of charge conservation. We treat heating and cooling by calculating the rate of removal or addition of energy to local radiation field associated with each of the processes affecting level populations (this is in contrast to the method where these were calculated via their effects on the electron thermal bath as in KM82). Heating therefore includes photoionization heating and Compton heating. The cooling term includes radiative recombination, bremsstrahlung, and radiative deexcitation of bound levels. Cooling due to recombination and radiative deexcitation is included only for the escaping fraction, as described elsewhere in this section.

In the most highly ionized regions of our models, the dominant heating process is electron recoil following Compton scattering. In the non-relativistic approximation the net heating rate may be written (Ross (1979))

$$n_e \Gamma_e = \frac{\sigma_T}{m_e c^2} \left(\int \varepsilon J_\varepsilon d\varepsilon - 4kT \int J_\varepsilon d\varepsilon \right) \tag{1}$$

Here σ_T is the Thomson cross section, n_e is the electron number density, T is the electron temperature, and J_ε is the local mean intensity in the radiation field. The first term in the brackets represents the heating of electrons by the X-rays, and the second term represents cooling of hot electrons by scattering with low energy photons.

The spectrum of photoelectron energies for each ion is found by convolving the radiation field, weighted by photoelectron energy, with the photoionization cross section (see, e.g., Osterbrock (1974)). The integral of this quantity provides the photoelectric heating rate.

The cooling rate due to radiative recombination is calculated by explicitly evaluating the quadrature over the recombination continuum spectrum for each recombining level, weighted by the escape fraction for that transition. The bremsstrahlung cooling rate is (Osterbrock (1974))

$$n_e\Gamma_e = 1.42 \times 10^{-27} T^{1/2} z^2 n_e n_z \text{ ergs cm}^{-3}\text{s}^{-1}, \tag{2}$$

where T is the electron temperature, n_e is the electron number density, z is the charge on the cooling ion, and n_z is the ion density.

2.5. Recombination Continuum Emission and Escape

In analogy with the line emission, recombination emission and cooling rates are calculated using the continuum level population n_∞ and the quantities calculated from the photoionization cross section and the Milne relation. The spontaneous recombination rates are given by

$$\alpha_i = \left(\frac{n_i}{n_{i+1} n_e}\right)^* \int_{\varepsilon_{th}}^{\infty} \frac{d\varepsilon}{\varepsilon} \frac{\varepsilon^3}{h^3 c^2} \sigma_{pi} e^{(\varepsilon_{th}-\varepsilon)/kT} \tag{3}$$

where $n_i{}^*$ is the LTE density of ion i, and n_e is the electron density. The continuum emissivity due to this process is given by

$$j_\varepsilon = n_{upper} n_e \left(\frac{n_i}{n_{i+1} n_e}\right)^* \frac{\varepsilon^3}{h^3 c^2} \sigma_{pi} e^{(\varepsilon_{th}-\varepsilon)/kT} \tag{4}$$

where n_{upper} is the number density of ions in the recombining level and σ_{pi} is the photoionization cross section. The cooling rate is given by the integral of this expression

over energy. These rates are calculated separately for each level included in the multilevel calculation.

In order to account for the suppression of rates due to emission and reabsorption of recombination continua, we multiply the rates and emissivities by an escape fraction given by:

$$P_{esc.,cont.} = \frac{1}{1000\tau_{cont.} + 1} \tag{5}$$

where $\tau_{cont.}$ is the optical depth at the threshold energy for the relevant transition. This factor is used to correct both the emission rate for the recombination events, and also the rates in the kinetic equations determining level populations etc, and has been found to give reasonably good fits to the results of more detailed calculations for the case of H II region models in which the Lyman continuum of hydrogen is optically thick (e.g. Harrington (1989)).

2.5.1. Line Emission and Escape

Since all level populations are calculated explicitly, line emissivities and cooling rates are calculated as a straightforward product of the population of the line upper level, the spontaneous transition probability and an escape fraction.

Line optical depths may be large in some nebular situations. Photons emitted near the centers of these lines are likely to be absorbed by the transition which emitted them and reemitted at a new frequency. This line scattering will repeat many times until the photon either escapes the gas, is destroyed by continuum photoabsorption or collisional deexcitation, or is degraded into longer wavelength photons which may then escape. Our treatment of resonance line transfer is based on the assumption of complete redistribution.

That is, we assume that there is no correlation of photon frequencies before and after each scattering event. This has been shown to be a good approximation for a wide variety of situations, particularly when the line profile is dominated by Doppler broadening. In this case, more accurate numerical simulations (e.g., Hummer and Rybicki (1971)) have shown that line scattering is restricted to a small spatial region near the point where the photons are emitted. Line photons first scatter to a frequency such that the gas cloud is optically thin and then escape in a single long flight. The probability of escape per scattering depends on the optical depth, τ_0 at the center of the line. For $1 \leq \tau_0 \leq 10^6$, the resonant trapping is effectively local. For $\tau_0 \geq 10^6$, the lines become optically thick in the damping wings, and the line escapes as a result of diffusion in both space and frequency. Since the scattering in the Doppler core is always dominated by complete redistribution, and since most of the lines in our models are optically thin in the wings, we assume that all line scattering takes place in the emission region.

We use the following expression for escape probability (Hollenbach and McKee (1978)):

$$P_{esc.,lines} = \frac{1}{\tau_{line}\sqrt{\pi}(1.2+b)} (\tau_{line} \geq 1) \tag{6}$$

$$P_{esc.,lines} = \frac{1 - e^{-2\tau_{line}}}{2\tau_{line}} (\tau_{line} \leq 1) \tag{7}$$

where

$$b = \frac{\sqrt{\log(\tau_{line})}}{1 + \tau_{line}/\tau_w} \tag{8}$$

τ_{line} is the optical depth at line center, and $\tau_w = 10^5$. Photons are removed from the line core by continuum opacity with a probability per scattering given by Hummer (1968):

$$P_{cont} = \beta F(\beta) \tag{9}$$

where $\beta = \kappa_{abs}/\kappa_0$, the ratio of continuum opacity to line center opacity, and

$$F(\beta) = 2\sqrt{(-\ln\beta\sqrt{\pi})} + \frac{1}{\beta}\mathrm{erfc}\left(\sqrt{-\ln\beta\sqrt{\pi}}\right) \tag{10}$$

Continuum opacity results from photoabsorption and Compton scattering, with probabilities

$$P_{abs} = (\kappa_{abs}/\kappa)P_{cont} \tag{11}$$

and

$$P_C = (\kappa_C/\kappa)P_{cont} \tag{12}$$

respectively. Here κ_{abs} is the photoabsorption opacity, κ_C is the Compton opacity, and $\kappa = \kappa_{abs} + \kappa_C$. Since the electron thermal velocity exceeds the ion velocity by $\sqrt{M/m_e}$, where m_e is the electron mass and M is the ion mass, Compton scattering is tantamount to escape, and the scattered radiation will appear as a Comptonized profile in the vicinity of the line core.

These rates enter in the calculation of the level populations via the net decay rate for excited levels, which is approximately $A_{ul}\min(1, P_{esc}(1 + P_{abs} + P_C))$. Collisional deexcitation is already explicitly treated as a deexcitation mechanism in our calculation of statistical equilibrium. The rate for line emission (i.e. local escape) and cooling is $A_{ul}P_{esc}$.

Photoexcitation of all levels by continuum fluorescence from the incident continuum is also included in our treatment of level populations. Fluorescent excitation by diffusely

emitted radiation, both continuum and lines, is not treated in the models presented in this paper, since it depends more sensitively on the treatment of radiation transfer. We defer a discussion of this process to a later paper.

The rates for line emission and the probabilities for the various resonance line escape and destruction probabilities depend on the state of the gas at each point in the cloud. The cooling function for the gas depends on the line escape probabilities, and the effects of line trapping must be incorporated in the solution for the temperature and ionization of the gas. Once the state of the gas at a given point has been determined, a fraction of the radiation emitted in each resonance line corresponding to the fractional probability of escape plus Compton scattering is assumed to escape the vicinity of the emission point. We treat the photoabsorption of this radiation as it traverses the rest of the cloud in the same way as the continuum at that energy.

2.5.2. Continuum Emission

Diffuse continuum radiation is emitted by three processes: thermal bremsstrahlung, radiative recombination, and two-photon decays of metastable levels. The thermal bremsstrahlung emissivity is given by Osterbrock (1974):

$$j_\varepsilon = \frac{1}{4\pi} n_z n_e \frac{32 Z^2 e^4 h}{3 m^2 c^3} \left(\frac{\pi h \nu_0}{3kT} \right)^{1/2} e^{-h\nu/kT} g_{ff}(T, Z, r) \qquad (13)$$

where T is the electron temperature, n_e is the electron abundance, Z is the charge on the most abundant ion, n_z is the abundance of that ion, and g_{ff} is a Gaunt factor (Karzas and Latter (1966)). For two photon decays, we adopt the distribution (Tucker and Koren (1971)):

$$H\left(\frac{\varepsilon}{\varepsilon_0}\right) = 12\left(\frac{\varepsilon}{\varepsilon_0}\right)^2\left(1-\frac{\varepsilon}{\varepsilon_0}\right) \tag{14}$$

where ε_0 is the excitation energy.

2.5.3. Continuum Transfer

The continuum radiation field is modified primarily by photoabsorption, for which the opacity, $\kappa(\varepsilon)$, is equal to the product of the ion abundance with the total photoionization cross section, summed over all levels.

A model is constructed by dividing the cloud into a set of concentric spherical shells. The radiation field incident on the innermost shell is the source spectrum. For each shell, starting with the innermost one, the ionization and temperature structure is calculated from the local balance equations using the radiation field incident on the inner surface. The attenuation of the incident radiation field by the shell is then calculated. The diffuse radiation emitted by the cloud is calculated using an expression of the formal solution of the equation of transfer:

$$L_\varepsilon = \int_{R_{inner}}^{R_{outer}} 4\pi R^2 j_\varepsilon(R) e^{-\tau_{cont.}(R,\varepsilon)} dR \tag{15}$$

where L_ε is the specific luminosity at the cloud boundary, $\tau_{cont.}(R,\varepsilon)$ is the optical depth from R to the boundary, and j_ε is the emissivity at the radius R. Since our models in general have two boundaries, we perform this calculation for radiation escaping at both the inner and outer cloud boundaries. This calculation is performed for each continuum energy bin, and separately for each line. In the case of the continuum, we construct a vector of emissivities, $j_\varepsilon(R)$ which includes contributions from the escaping fraction from all the levels which affect each energy. For the lines, the emissivity used in this equation is the

escaping fraction for that line.

2.5.4. Algorithm

Construction of a model of an X-ray illuminated cloud consists of the simultaneous solution of the local balance equations. The radiative transfer equation is solved for both the continuum and for the lines that escape the region near the point of emission. The large number of ions in the calculation results in many ionization edges that may affect the radiation field. We solve the transfer equation on a frequency grid that includes a total of 5000 continuum grid points with even logarithmic spacing in energy from 0.01 eV to 40 keV resulting in a limiting resolution of 0.3 %, corresponding to, e.g. 20 eV at 7 keV. We calculate the luminosities of ~10000 spectral lines and solve the continuum transfer equation individually for each of these. The emissivity of each line at each point is the product of the emissivity and the local escape fraction for that line. The continuum opacity for each line is the opacity calculated for the energy bin that contains the line. This procedure is repeated for each successive shell with increasing radius.

Calculation of the escape of the diffuse radiation field depends on a knowledge of the optical depths of the cloud from any point to both the inner and outer boundaries. Since these are not known a priori we iteratively calculate the cloud structure by stepping through the radial shells at least 3 times. For the initial pass through the shells we assume that the optical depths in the outward direction are zero. This procedure is found to converge satisfactorily within 3-5 passes for most problems of interest. This procedure is tantamount to the "Λ-iteration" procedure familiar from stellar atmospheres, and must suffer from the same convergence problems when applied to problems with large optical depths. These problems are reduced in our case by the use of escape probabilities rather than a full integration of the equation of transfer.

2.6. Atomic Processes

Here we summarize the most important data sources adopted for the calculations. These are discussed in greater detail, along with a description of the fitting formulas and assumptions, in Bautista and Kallman (2000a).

2.6.1. Photoionization

Photoionization rates are obtained by convolving the radiation field with the photoionization cross section. Cross sections are included for all levels of every ion for a wide range of photon energies occurring in our model. The cross sections where taken from the Opacity Project (Seaton, et al., (1993), Cunto et al., (1993)), then averaged over resonances as in Bautista et al. (1998a) and split over fine structure according to statistical weights.

For inner shell photoionization not yet available from the opacity project we use the cross sections of Verner and Yakovlev (1995). Inner shell ionization in X-ray illuminated clouds is enhanced by Auger cascades. This process can result in the ejection of up to eight extra electrons (in the case of iron) in addition to the original photoelectron. We include this effect by treating each inner shell ionization/auger event as a rate connecting the ground state of one ion with another level of an ion (in general not adjacent to the initial ion). The rates for inner shell ionization/auger processes are calculated using the relative probabilities of the various possible outcomes of an inner shell ionization event from Kaastra and Mewe (1989). These yields are multiplied by the appropriate inner shell photoionization cross section in order to calculate a rate for each inner shell ionization/Auger cascade individually. Our level scheme also includes levels with inner shell vacancies, which are populated by inner shell/Auger events. Populations of these levels are calculated in the

customary way, and the decays from these levels produce inner shell fluorescence lines.

2.6.2. Collisional Ionization

Ionization by electron collisions is important if the gas temperature approaches a fraction of the ionization threshold energy of the most abundant ions in the gas. Although most of the problems for which XSTAR is designed do not satisfy this criterion, we include this process in order to accurately treat the inverse process, and in order to compare with calculations specifically tailored for coronal situations. For ground states we include the rates from Raymond and Smith (1986) for elements other than iron, and from Arnaud and Raymond (1992) for iron. Collisional ionization from excited levels may also be important to the ionization balance. We include ionization rates for all excited levels of every ion using approximate formulae by D. Sampson and coworkers (Zhang and Sampson (1987)). 3-body recombination rates to all levels are calculated from the collisional ionization rates using the detailed balance principle.

2.6.3. Recombination

Radiative and dielectronic recombination rates to all spectroscopic levels are calculated from the photoionization cross sections using the Milne relation. We include both spontaneous and stimulated recombination caused by the illuminating radiation. Stimulated recombination by the locally emitted radiation is not treated explicitly, although its effect is taken into account in an approximate way by suppressing a fraction of the spontaneous recombinations using the escape probability described earlier in this section. Recombination onto the superlevels is calculated in order to account for the difference between the sum over all spectroscopic levels and the total ion recombination as given by Nahar and coworkers

(Nahar (1999), Nahar (2000)) where available and Aldrovandi and Pequignot (1973) for species other than iron ions and ions in the H and He isoelectronic sequences. For iron we use total rates from Arnaud and Raymond (1992). For H and He-like ions the total recombination rates were calculated by Bautista et al. (1998b) and Bautista and Kallman (2000b).

2.6.4. Collisional Excitation and Radiative Transition Probabilities

Collision strengths and A-values were collected from a large number of sources. Particularly important for this compilation were the CHIANTI data base (Dere, et al. (1997)) for X-ray and EUV lines, and the extensive R-matrix calculations by the Iron Project (Hummer et al. (1993)).

2.6.5. Charge Transfer

Rates for charge transfer reactions are taken from Butler Heil and Dalgarno (1980). For highly charged ions, where accurate calculations do not exist, we scale the rates along isonuclear sequences, assuming that the cross section is proportional to the square of the total residual charge transfer reaction of O II with H (Field and Steigman (1971)). This is similar to the scaling for q 4 employed by Ferland, et al. 1997; we are in the process of evaluating the differences between these treatments and will present a comparison in a future paper. Charge transfer is only important in the regions of the clouds where neutral fraction of hydrogen or helium exceeds 0.01 or so. This turns out to be close or beyond the hydrogen ionization front for most model clouds, and so does not affect the sample model results shown in this paper.

2.7. Other Features

Other features of XSTAR which are intended to facilitate its use by the general astronomical community include making it part of the FTOOL software package circulated by the GSFC Laboratory for High Energy Astrophysics. Features include: parameter file user interface, support for users and installation, compatibility with other analysis tools such as XSPEC and output files in FITS format. Also the code has been structured in order to allow a clean separation between atomic data and computation of rates, which facilitates swapping and intercomparison of atomic datasets.

3. Sample Results: Low Density

Although many of the results of XSTAR v.2 calculations are similar to those described in KM82, we present as background some results of simple models which illustrate the behavior of photoionized gas and which display some of the adopted atomic rates and cross sections. All of the results presented in this and the next section are for optically thin models; we defer a discussion of radiation transfer effects to a later paper.

3.1. Atomic Rates and Cross Sections

We begin by displaying some of the atomic rates which are notable due to their departure from previous work, or to their effects on the model results. Figure 1 shows the ground state photoionization cross sections we adopt. Each panel contains the cross sections for a given element, with various curves for the respective ions. In most cases the various subshells of a given ion are also plotted as separate non-overlapping curves. Resonance structure near threshold of outer shells is apparent, particularly in ions with $Z \geq 10$. The photoionization cross sections from many excited levels also show resonance structure. This

is illustrated in Figure 2, which shows a few of the excited level cross sections for O VII. Notable are the resonance features near 650 eV, corresponding to the 1-2 transitions in the O VIII ion. Although cross sections with comparable resolution are available for many ions from the opacity project, we adopt Gaussian average fits to these for the great majority of excited levels. For O VII we include all available cross sections at high resolution for ground and excited levels with principle quantum number $n \leq 4$ in order to illustrate the potential importance of the resonance structures in observed spectra.

Ground state collisional ionization rate coefficients are shown in Figure 3. Each panel contains the rates for a given element as a function of temperature.

Figure 4 shows the radiative recombination rates we adopt. We emphasize that these are calculated by performing a Milne integral (equation 3) over the photoionization cross section for each of the bound levels of the recombined ion, and then summing over those rates. This is in contrast to the more typical nebular treatment in which such a sum is fit to an analytic formula as was done by, e.g. Aldrovandi and Pequignot (1973), and has the advantage that it causes all rates to go to detailed balance ratios in the proper limit. Each panel in Figure 4 contains the rates for a given element. Also shown, as the dashed curves, are the rates adopted in XSTAR v.1, i.e. those of Gould and Thakur (1970) (hydrogenic ions) Arnaud and Raymond (1992) (for iron), and Aldrovandi and Pequignot (1973) (all others). Differences are prominent for elements such as C, O, and Fe, and primarily reflect differences between the previous dielectronic recombination rates and those adopted here (e.g. Nahar (2000) and references therein).

3.2. Ionization Balance

In general, the state of the gas depends on both the temperature, via the recombination rates and collisional ionization rates, and on the radiation field, via the photoionization rates. This combined dependence makes a display of the ionization balance cumbersome in the absence of some other simplifying assumption. Figure 5 shows the ionization balance in the coronal case, i.e. when the radiation field is negligible, as a function of temperature. This can be compared with other similar calculations such as, e.g. Arnaud and Rothenflug (1985).

3.3. Heating and cooling rates

A by-product of the ionization and excitation balance is the emissivity and opacity of the gas, which correspond to the net heating and cooling rates. Figure 6 shows the heating and cooling rates as a function of temperature and ionization parameter for the various elements. Heating rates are shown as solid curves, cooling rates as dashed curves. Rates assume solar abundances (Grevesse, Noels and Sauval (1996)), and are given in units of erg s^{-1} cm^{+3} per H nucleus. Different curves correspond to ionization parameters log(ξ)=0,1,2,3,4 for an ε^{-1} power law ionizing spectrum. Fewer curves appear in some panels owing to pile up at low ionization parameters for elements such as carbon, while for H and He, the log$\xi \geq 2$ curves fall below the range plotted. These are calculated in the limit of low gas density, n=1 cm^{-3}.

A coronal plasma cools more efficiently, in general, than a photoionized plamsa since the ionization state is lower at a given temperature. Figure 7 shows the cooling rate as a function of temperature for such a plasma. Comparison of these rates with the results of Figure 6 shows similarity with the cooling rate at the lowest ionization parameter plotted

there ($\log\xi=0$), although the coronal rates are generally larger at low temperatures. This is a reflection of the fact that at $\log\xi=0$ there is significant photoionization of the neutral and near-neutral species.

3.4. Thermal Balance Calculation

When the condition of thermal equilibrium is imposed, then the temperature is determined as a function of ionization parameter for a photoionized plasma. Figure 8 shows the ionization and temperature of an optically thin low density photoionized gas with a ε^{-1} ionizing continuum, as a function of ionization parameter. This can be compared with the results of KM82, model 7 (although that model was not optically thin for $\log(\xi)\leq 2$). The current model is significantly more highly ionized; the ionization parameter where the abundances of O VII and VIII reach their maximum is lower by 0.5 dex in the current models. The temperature calculated here is lower; this may be due to a different choice of low and high energy spectral cutoffs which affect the Compton equilibrium temperature.

4. Sample Results: High Density

At high densities, various physical processes become important which can affect the ionization and thermal balance. These include:

Lowering of the continuum, in which collisional ionization from highly excited levels (i.e. superlevels) results in a net reduction in the effective reccombination rates. This effect is only included for H and He-like ions in our calculations. This process is most important at low temperatures. A competing effect is collisional deexcitation from superlevels, but this turns out to be less important than continuum lowering.

3-body recombination results in a net increase in total recombination rate. In our models we include collisional ionization and 3-body recombination from essentially all levels, although this process is generally more important for levels closest to the continuum.

At high densities the spectroscopic level populations in the recombining ion can approach their LTE values, leading to enhanced collisional ionization from these levels and a decrease in the total recombination. This turns out to be unimportant for most ions at the densities and temperatures we consider.

In a photoionized plasma the incident photon flux must be very large if the density is high and the ionization parameter is within the conventional range. Such high photon fluxes can lead to large enhancements in the recombination rate via stimulated recombination.

4.1. Density dependent recombination rates

The effects of density on recombination rates are illustrated in figure 9, which shows recombination rate as a function of density for various ions of H, He and O. The curves correspond to temperatures logarithmically spaced between 10^4K and 10^7 K, and the dashed curve shows the XSTAR v.1 value. Stimulated recombination can cause large enhancements in the rates at high density, but its effects are dependent on the shape of the assumed ionizing spectrum; therefore it has been excluded from the results until the end of this section for illustrative purposes. In the H and He-like ions the lowering of the continuum is apparent at moderate densities, and the effect of 3-body recombination is apparent in H I and He I at the highest densities. This is an illustration of the fact that, at a given density, 3-body recombination is greater for ions with lower free charge, and is greater at lower temperature (Bautista et al. (1998b)). The calculations shown in this figure were done at a fixed ionization parameter of $\log(\xi)=2$ with an ε^{-1} ionizing continuum. As a result the

lower ionization stages, of oxygen, O I, O II, and O III have low abundance and are not included in the full multilevel matrix calculation and their recombination rates are treated using the total rates shown in Figure 3. Other ions show the effects of continuum lowering, which causes a decrease in rate by a factor of up to $\sim$ a few beginning at densities greater than 10^6–10^8.

4.2. Level populations vs. density

In addition to enhancing the total recombination rate, high densities enhance the importance of collisional processes relative to radiative processes in bound-bound transitions. Level populations approach their LTE values, which may greatly exceed the recombination values for levels with dipole allowed decays. This is illustrated in Figure 10, which shows the ratio of level populations to LTE populations (departure coefficients) relative to the continuum as functions of density for H I at log(ξ)=-5 and T=10^4K (panel a) and for O VIII at log(ξ)=-5 and T=10^6K (panel b). Departure coefficients of all bound spectroscopic levels decrease proportional to density, approaching asymptotic values at densities greater than 10^{17} cm^{-3}. The superlevels exhibit slower dependence on density, reflecting the fact that they are likely to be in LTE with the continuum at lower density than the spectroscopic levels.

4.3. Heating-cooling vs. density

Heating and cooling rates depend on density via the ionization balance and via the rates for the heating and cooling per ion. In the previous subsection we have shown that at the highest densities we consider the recombination rates can be enhanced by 3 body recombination, or reduced, by continuum lowering and collisional ionization. The former

process is dominant at high densities for H I and He I, while the latter dominates for moderate densities for other ions. Since the thermal balance in a photoionized gas is dominated by H and He when the ionization parameter is low (i.e. $\log(\xi) \leq 1$), and by more highly charged ions at higher ξ, we expect the heating and cooling to be affected differently at high densities in the two different regimes. Although the dependence of cooling rate on ionization balance at low densities is not generally monotonic (c.f. figure 6), for many ions the heating rate is greater at lower ionization parameter. The per ion heating rate depends on the photon flux rather than the gas density, while the per ion cooling rate is suppressed by collisional deexcitation. Figure 11 shows the dependence of heating and cooling rates on density and temperature, in a form analogous to that of figure 10. Curves show cooling (dashed) and heating (solid) rates at 5 temperatures spaced logarithmically between between 10^4K and 10^7 K, for $\log(\xi)$=2 and a ε^{-1} power law ionizing spectrum. For highly ionized species heating rates are decrease slightly with density, while cooling rates increase. H I and He I behave in the opposite way, owing to the increase in recombination (which increases the neutral fraction and hence the photoionization heating) and to the collisional suppression of radiative decays (which decreases the net radiative cooling).

4.4. Thermal Equilibrium

Figure 12 shows the results of a thermal balance calculation of an optically thin photoionized gas as a function of density and ionization parameter. The curves correspond to ionization parameters $\log(\xi)$=4,3,2,1 for the same power law ionizing spectrum used previously. This demonstrates that the net effect of higher densities is an increase in temperature at the highest densities and lowest temperatures, and a decrease in temperature at lower density and higher temperature, for the reasons listed in the previous section. We emphasize that the quantitative value of the temperature, particularly for high ionization

parameters and/or temperatures greater than 10^7 K or so, depends on the detailed shape of the ionizing spectrum over all energies, owing to the possible importance of Compton heating and cooling (the spectral dependence of the effects of stimulated recombination, again, have been excluded from these results).

4.5. Ionization distribution, high n

Figure 13 shows the ionization and thermal balance of an optically thin photoionized gas analogous to that shown in Figure 8, but at a density of 10^{17} cm^{-3}. Comparison shows that the high density results in generally higher ionization state for most elements at high ionization parameter, owing to the reduction in the net recombination rate. At the same time, the temperature is slightly lower, as described in the previous subsection. The opposite is true at the low ionization parameter extreme of figure 13 – the temperature is slightly greater than in figure 9 due to the enhanced recombination rates of H and He I at high densities.

4.6. Warm absorber, high density

High densities also affect the absorption and emission spectra of photoionized plasmas. Figure 14 shows a comparison of a warm absorber spectrum at densities of 10^4 cm^{-3} (panel a) and 10^{17} cm^{-3} (panel b) due to oxygen in the 0.5-1 keV energy range. The ionization parameter is $\log(\xi)=2$ and the temperature is 10^5K. In the high density case there is a prominent absorption structure near 0.65 keV, associated with resonances in the photoionization cross sections from the 1s2s configurations in OVII. These resonances are apparent in the cross sections shown in figure 2, and they appear in opacity due to the build-up of excited level populations at high densitiies. Such features are potentially

observable in the spectra of astrophysical X-ray sources such as the partially ionized absorbers associated with Seyfert galaxies (e.g. George et al. (1998)) if these objects contain gas at densities comparable to those considered here.

4.7. Recombination emission, high density

Figure 15 shows a comparison of the emission spectrum at densities of 10^4 cm^{-3} (panel a) and 10^{17} cm^{-3} (panel b) due to oxygen in the 0.5-1 keV energy range. The ionization parameter is log(ξ)=2 and the temperature is 10^5K. In the high density case the ratio of continuum to line emission is reduced, and the ratios of the He-like lines is changed from the familiar low-density case in which the forbidden/intercombination line ratio is large at low density to values $\sim$1 at high density.

4.8. The effects of stimulated recombination

So far in this section we have artificially excluded the effects of stimulated recombination (by manually setting the rates to zero when calculating total recombination). We illustrate the effect of relaxing this condition in figure 16, which is the equivalent of figure 9 (recombination rates vs. density) but with stimulated recombination included. Again the ionizing spectrum is a ε^{-1} power law, which has strong flux at the lowest photon energies. Comparison of figures 16 and 9 shows that the rates are greatly enhanced at high densities, and this enhancement is greatest for ions with lowest ionization potentials. This is due to the influence of the low energy photons on the stimulated recombination rate, and a different spectral shape (e.g. a blackbody) would produce a different distribution of recombination with charge state at high densities.

5. Summary

In this paper we have presented new models for the atomic spectra of hot, ionized gases which incorporate some of the physical processes needed to accurately describe the conditions in high density astrophysical sources. Chief among these is the inclusion of many collisional transitions which allow the level populations to approach LTE conditions in the proper limit. Radiative transitions are also included such that the LTE populations are obtained in the limit of Plankian (incident) radiation field and no escape of diffuse radiation. All atomic rates and constants have been recently evaluated in an attempt to use the most accurate and complete possible values. The code is portable and documented and it is freely available on the web and as part of the FTOOLS software package.

Sample results have been presented which illustrate the model behavior under the conditions familiar from previous studies of nebulae, in addition to exploring the effects of high gas densities. In the latter case we have demonstrated that the dominant effect at the highest densities we consider is that of 3-body recombination, which results in a temperature which exceeds the low density values by factors $\geq$10. Such high density gas is expected to be discernible by its X-ray spectral signatures, including emission line ratios and line/continuum ratios, and absorption from excited levels. In future papers we plan to explore the effects of radiative transfer on our model results, and the applications of these models to observed high resolution X-ray spectra.

This work could not have been carried out without encouragement from Julian Krolik, and programming support from Tom Bridgman and James Peachey. The work has been funded by NASA grant NAG 5-1732.

REFERENCES

Aldrovandi, S., and Pequignot, D., 1973 Astr. Ap. 25, 137; 1976 47, 321

Arnaud, M., and Rothenflug, R., 1985, A. and A. Supp. 60 425

Arnaud M., and Raymond, J., 1992, Ap. J., 395, 398

Bambynek W., et al.1972, Rev. Mod. Phys. 44, 716

Barfield, W., Koontz, G. and Huebner, W., 1972, JQSRT, 12, 1409

Bautista, M., Romano, P., and Pradhan, K., 1998a Ap. J. Supp., 118, 259

Bautista, M., Kallman, T., Angelini, L., Liedahl, D., and Smits, D.,, 1998 Ap. J., 509, 848

Bautista, M., and Kallman, T., 2000a, Ap. J. submitted.

Bautista, M., and Kallman, T., 2000b, Ap. J. in press.

Butler, S., Heil, T.G., and Dalgarno, A., 1980, Ap. J., 241, 442

Cunto, et al., 1993, A and A, 275, L5

Dalgarno, A. and Butler, S. , 1978, Comments At. Mol. Phys., 7, 129

Dalgarno, A., Heil, T., and Butler, S., 1981, Ap. J., 245, 793

Davidson, K., and Netzer, H., 1979, Rev. Mod. Phys., 51, 715

Dere, K. P., et al., 1997, A and A S, 125, 149.

DDumont, A., Abrassart, A., and Collin, S.., 2000, A and A, 357, 823.

Ferland, G., 1996, University of Kentucky Internal Report.

Ferland, G., et al., 1997, Ap. J., Lett., 481, L115

Field, G., and Steigman, G., 1971, Ap. J., 166, 59

George, I., et al., 1998, Ap. J. Supp. 114, 73

Gould, G. and Thakur, R., 1970, Ann. Phys., 61, 351

Grevesse, N., Noels, A., and Sauval, A., 1996, in "Cosmic Abundances" ASP Conference Series, 99, S. Holt and G. Sonneborn, eds.

Halpern, J., and Grindlay, J., 1980, Ap. J., 242, 1041

Hatchett, S., Buff, J., and McCray, R., 1976, Ap. J., 206, 847

Harrington, J.P., 1989, proceedings of the 131st symposium of the IAU held in Mexico City, Mexico, october 5-9, 1987. Ed S. Torres-Peimbert. Planetary Nebulae, 157-166

Hollenbach, D., and McKee, C., 1978, Ap. J. Supp., 41,555

Hummer, D., 1968, MNRAS, 138, 73

Hummer, D., et al., 1993, A and A, 279, 298

Hummer, D., and Rybicki, G., 1971, Ann. Rev. Astr. Ap., 9, 237

Illarionov, A., et al. 1979. Ap. J., 228, 279

Kallman, T., and McCray, R., 1980, Ap. J., 242, 615

Kaastra, J., and Mewe, R., 1989, A and A Supp., 97,443

Kallman, T., and McCray, R., 1982, Ap. J. Supp., 50, 49

Kallman 1983, Ap. J., 280, 269

Karzas and Latter, 1966

Krolik, J., McKee, C., and Tarter, C. B., 1981, Ap. J., 249, 422

McCray, R., Wright, C., and Hatchett, S., 1977, Ap. J., 211, 29

Mendosa 1982)

Nahar, S., 1999, Ap. J. Supp., 120, 131

Nahar, S., 2000, in "Atomic Data Needs for X-ray Astronomy", M.A. Bautista, T.R. Kallman, and A.K. Pradhan, eds., NASA special pub., http://heasarc.gsfc.nasa.gov/docs/heasarc/atomic/proceed.html

Seaton, M., et al., 1993, Rev. Mex. Astron. Astrofis., 23, 19

Osterbrock, D., 1974, Astrophysics of Gaseous Nebulae San Francisco: Feeman)

Press, W. et al., "Numerical Recipes"

Raymond and Smith 1986

Ross, R., 1979, Ap. J., 233, 334

Tarter, C. B., Tucker, W, and Salpeter, E., 1969, Ap. J., 156, 943

Tucker, W., and Koren, M., 1971, Ap. J., 168, 283

Verner, D. A., and Yakovlev, D. G., 1995, A and A S, 109, 125

Zhang, H., and Sampson, D., 1987 Ap. J. Supp., 63, 487

Press - Numerical Recipes

This manuscript was prepared with the AAS LaTeX macros v4.0.

Fig. 1.— Ground state photoionization cross sections (cm^2) vs. photon energy plotted for various elements. Curves correspond to ions with increasing ionization potential.

Fig. 2.— Photoionization cross sections (cm^2) vs. photon energy plotted for various levels of O VII in the energy range between 500 eV and 1 keV. Resonance structure in the excited level cross sections is apparent near 650 eV

Fig. 3.— Ground state collisional ionization rate coefficient (in $cm^3\ s^{-1}$) vs. gas temperature for various elements.

Fig. 4.— Total recombination rate coefficient (in $cm^3\ s^{-1}$) vs. gas temperature for various elements. Solid curves corresponds to rates adopted here (described in text). Dashed curves correspond to rates from XSTAR v.1 (references given in text)

Fig. 5.— Coronal ion fractions (ionization balance) vs. temperature

Fig. 6.— Heating and cooling rates as a function of temperature and ionization parameter for the various elements. Heating rates are shown as solid curves, cooling rates as dashed curves. Rates assume solar abundances, and are given in units of erg s^{-1} cm^3 per H nucleus. Different curves correspond to ionization parameters $\log(\xi)$=0,1,2,3,4,5 for an ε^{-1} power law ionizing spectrum.

Fig. 7.— Cooling rates as a function of temperature for the various elements under the assumption of coronal equilibrium. Rates assume solar abundances, and are given in units of erg s^{-1} cm^3 per H nucleus.

Fig. 8.— Ion fractions and temperature of an optically thin low density photoionized gas, as a function of ionization parameter for an ε^{-1} power law ionizing spectrum.

Fig. 9.— Recombination rate coefficient as a function of density for various ions of H, He and O. The curves correspond to temperatures logarithmically spaced between 10^4K and 10^7

K, and the dashed curve shows the XSTAR v.1 value.

Fig. 10.— Deaprture coefficients relative to continuum as functions of density for H I at $\log(\xi)$=-5 and T=10^4K (panel a) and for O VIII at $\log(\xi)$=-5 and T=10^6K (panel b)

Fig. 11.— Heating and cooling rates vs. density and temperature. Shown are cooling (dashed) and heating (solid) rates at 5 temperature spaced logarithmically between between 10^4K and 10^7 K, for $\log(\xi)$=2 and a ε^{-1} power law ionizing spectrum.

Fig. 12.— Temperature of an optically thin photoionized gas as a function of density and ionization parameter. The curves correspond to ionization parameters $\log(\xi)$=5,4,3,2,1 for the same power law ionizing spectrum used previously.

Fig. 13.— Ionization and thermal balance of an optically thin photoionized gas analogous to that shown in Figure 8, but at a density of 10^{16} cm^{-3}.

Fig. 14.— Warm absorber spectrum at densities of 10^4 cm^{-3} (panel a) and at 10^{17} cm^{-3} (panel b) due to oxygen in the 0.5-1 keV energy range. The ionization parameter is $\log(\xi)$=2 and the temperature is 10^5K.

Fig. 15.— Emission spectrum due to oxygen in the 0.5-1 keV energy range at density of 10^4 cm^{-3} (panel a) and at density of 10^{17} cm^{-3} (panel b). The ionization parameter is $\log(\xi)$=2 and the temperature is 10^5K.

Fig. 16.— Same as figure 9, but including stimulated recombination for a ε^{-1} power law ionizing spectrum.

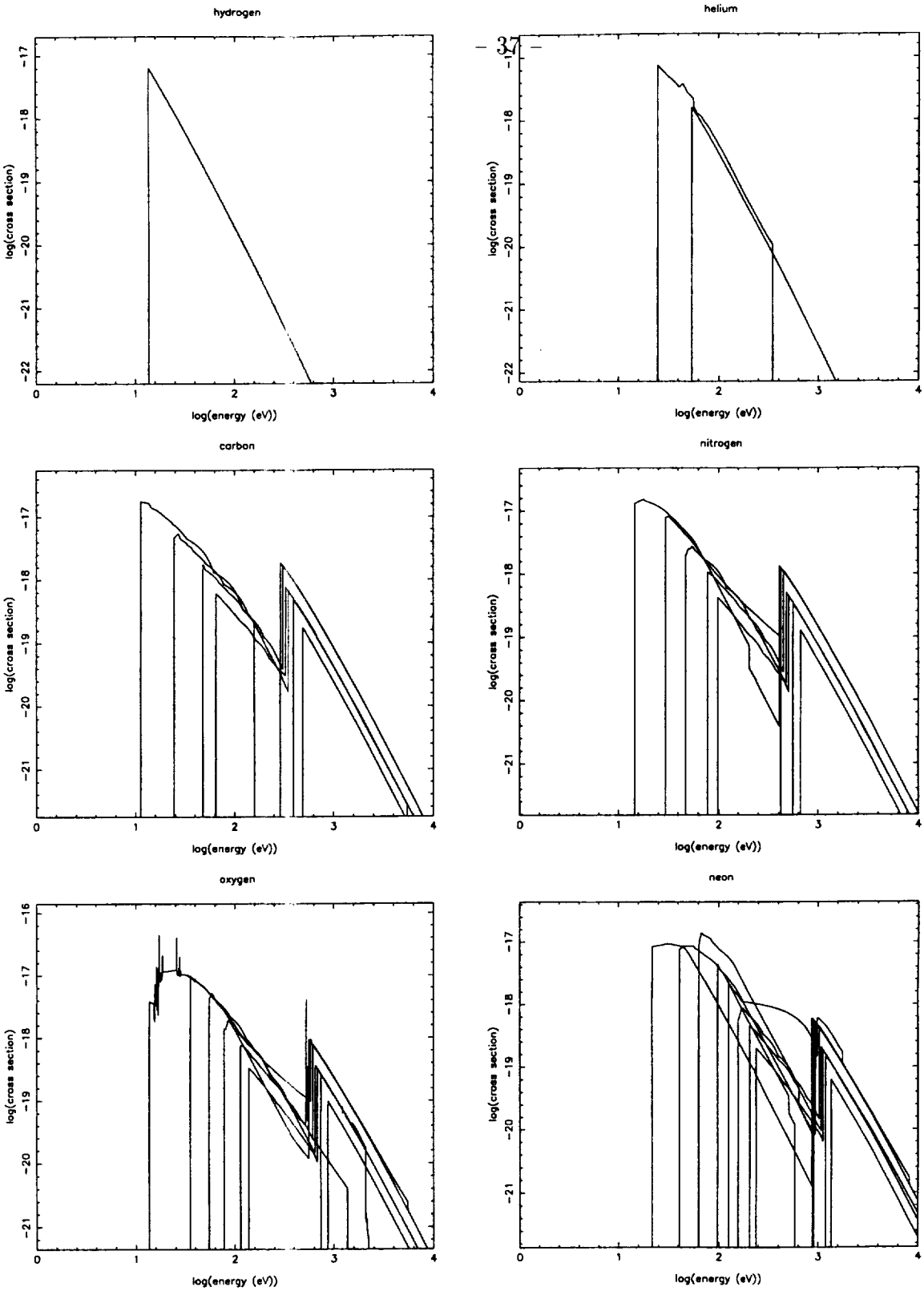
hydrogen
helium
carbon
nitrogen
oxygen
neon
log(cross section)
log(energy (eV))

Fig. 1.— a

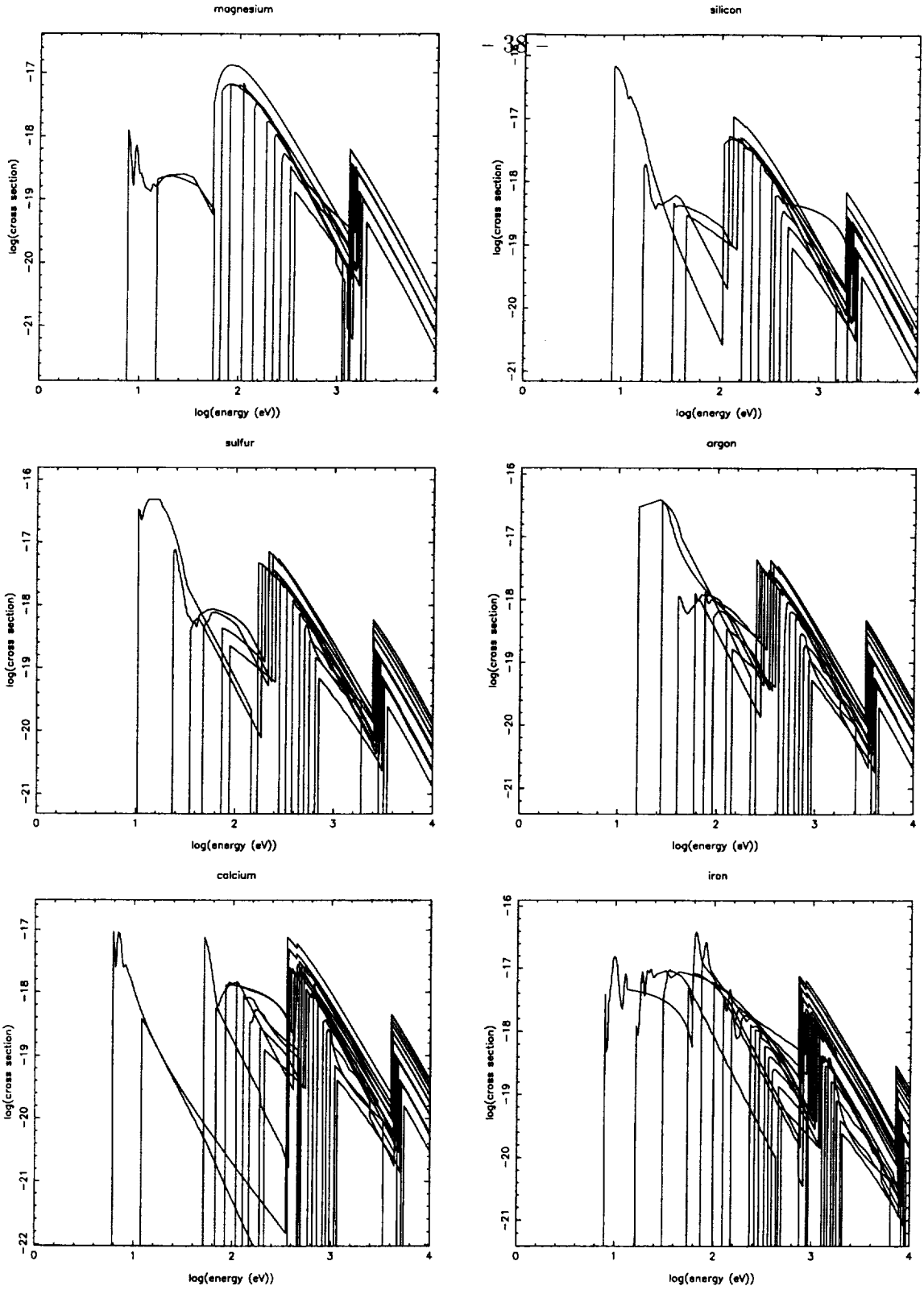
magnesium
silicon
sulfur
argon
calcium
iron
log(cross section)
log(energy (eV))

Fig. 1.— b

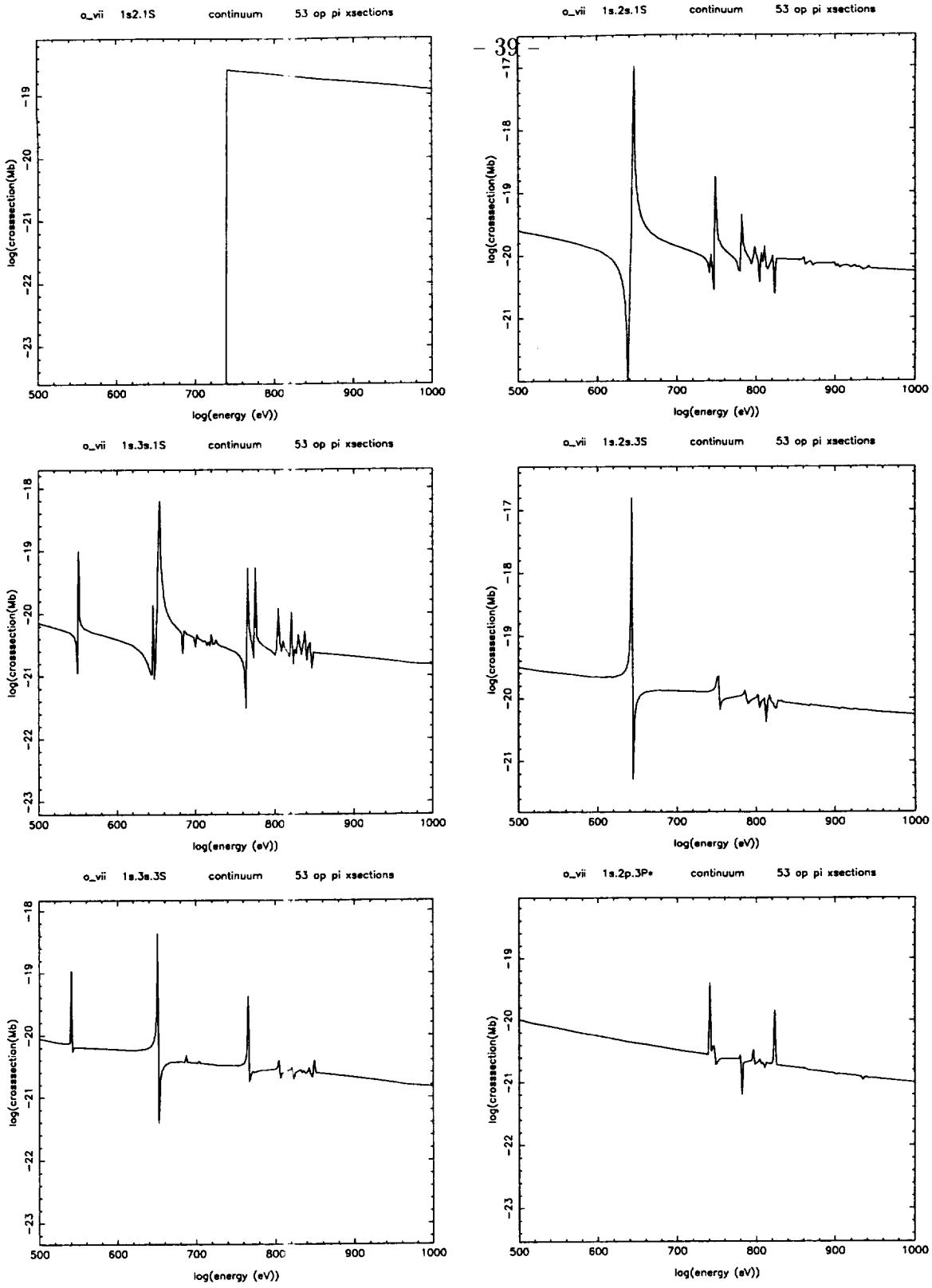
o_vii 1s2.1S continuum 53 op pi xsections
o_vii 1s.2s.1S continuum 53 op pi xsections
o_vii 1s.3s.1S continuum 53 op pi xsections
o_vii 1s.2s.3S continuum 53 op pi xsections
o_vii 1s.3s.3S continuum 53 op pi xsections
o_vii 1s.2p.3P* continuum 53 op pi xsections
log(crossection(Mb)
log(energy (eV))

Fig. 2.—

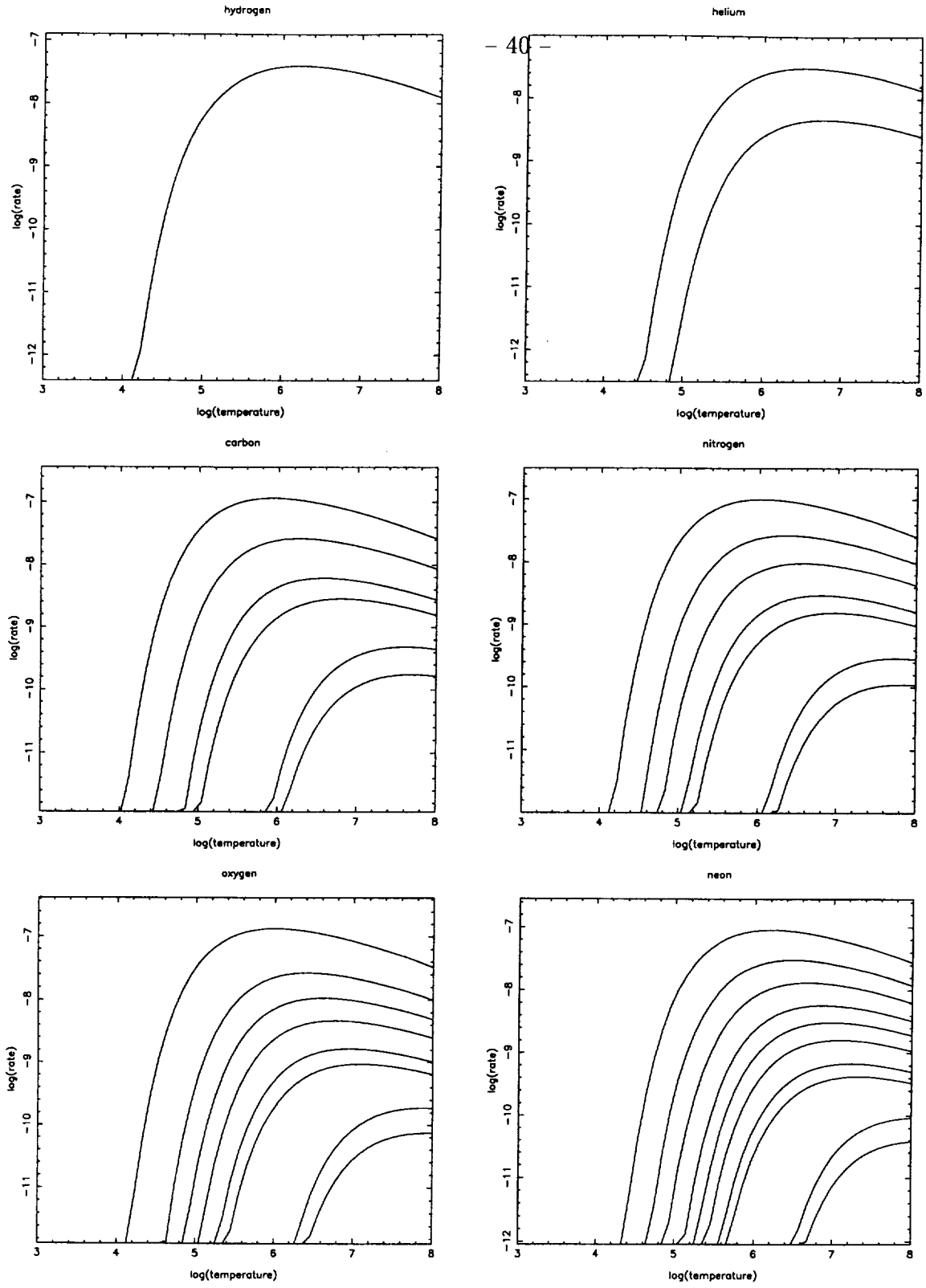
hydrogen
helium
carbon
nitrogen
oxygen
neon
log(rate)
log(temperature)

Fig. 3.— a

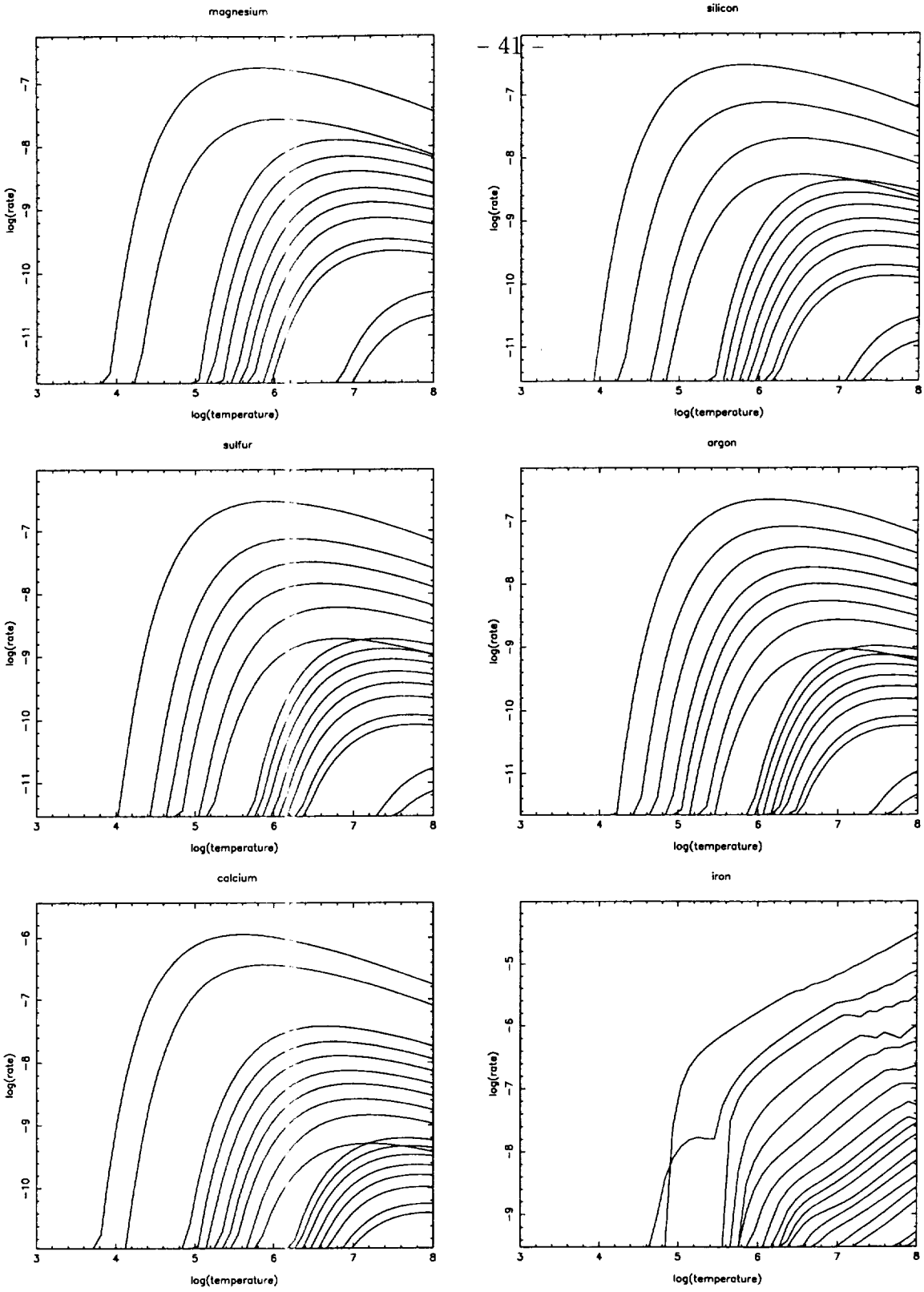
magnesium
silicon
sulfur
argon
calcium
iron
log(rate)
log(temperature)

Fig. 3.— b

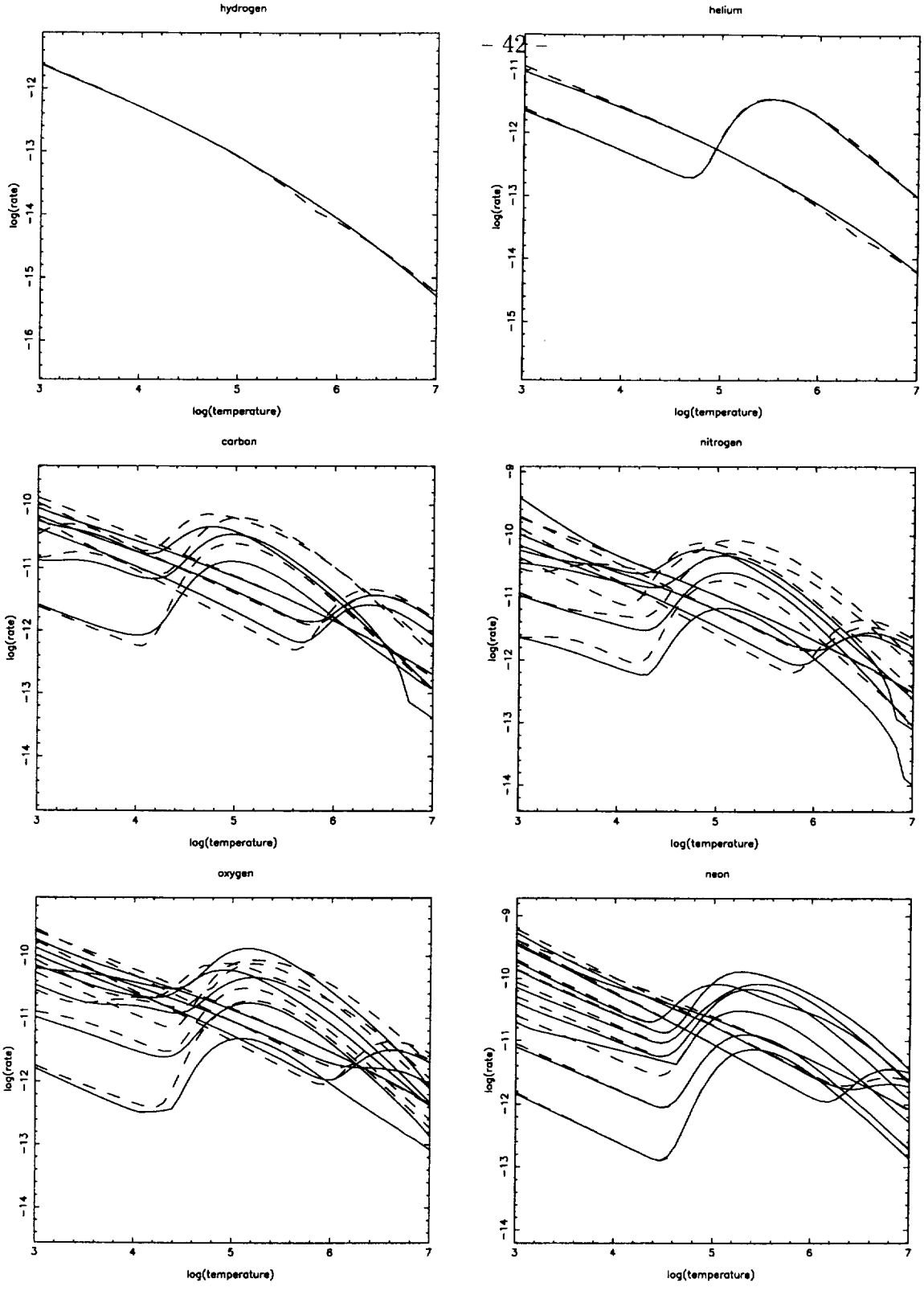
hydrogen
helium
carbon
nitrogen
oxygen
neon
log(rate)
log(temperature)

Fig. 4.— a

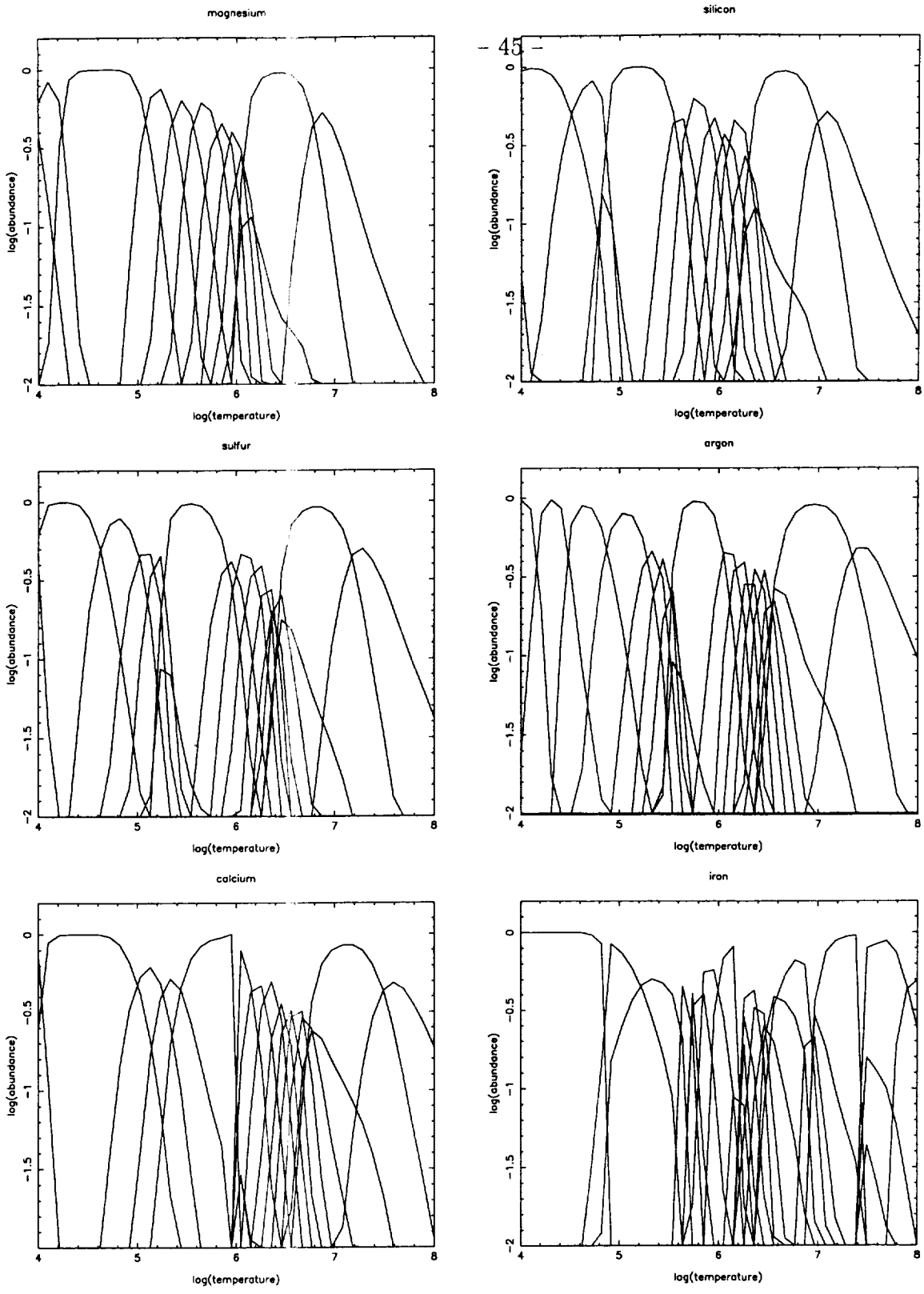
magnesium
silicon
sulfur
argon
calcium
iron
log(abundance)
log(temperature)
0
−0.5
−1
−1.5
−2
4
5
6
7
8

Fig. 5.— b

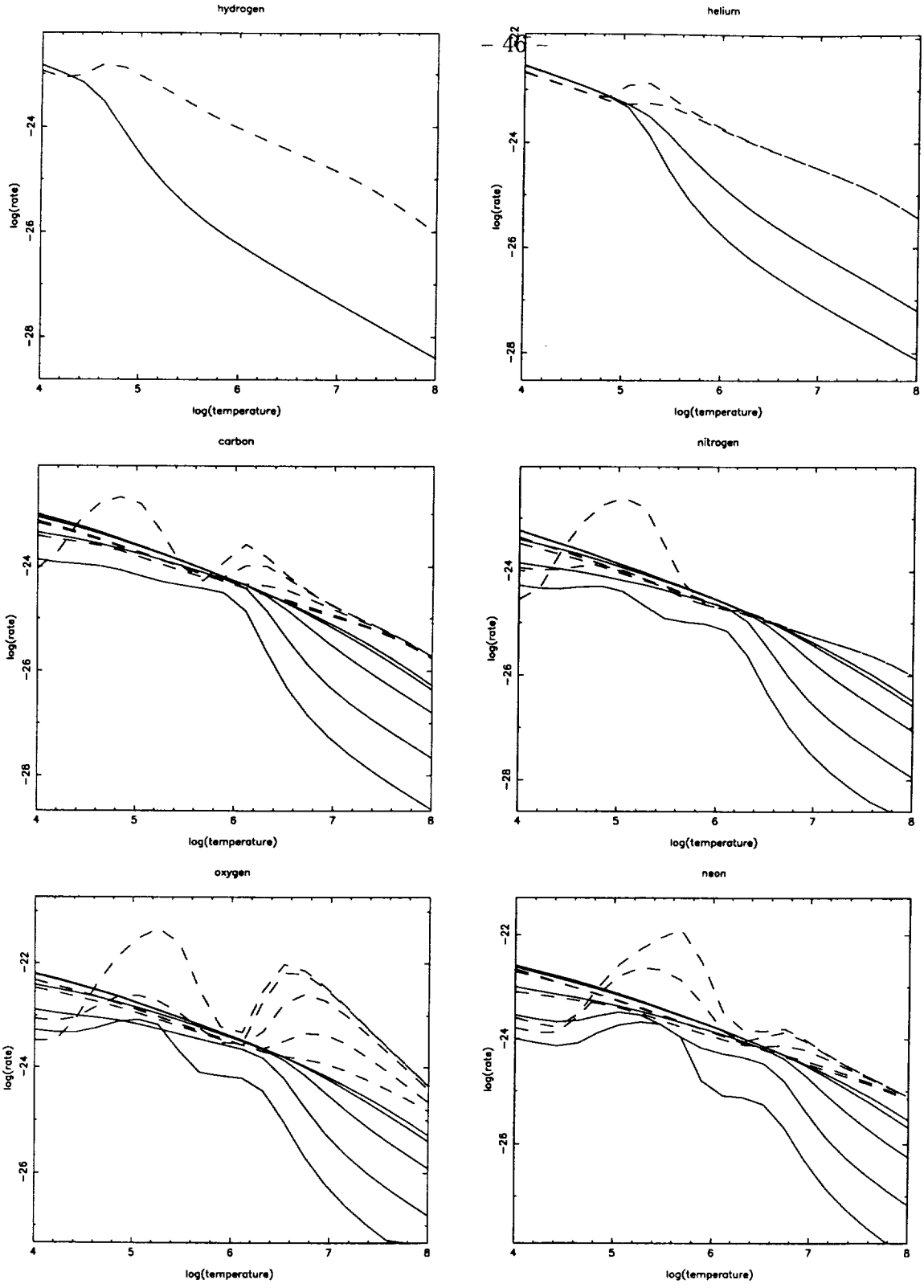
hydrogen
helium
carbon
nitrogen
oxygen
neon
log(rate)
log(temperature)

Fig. 6.— a

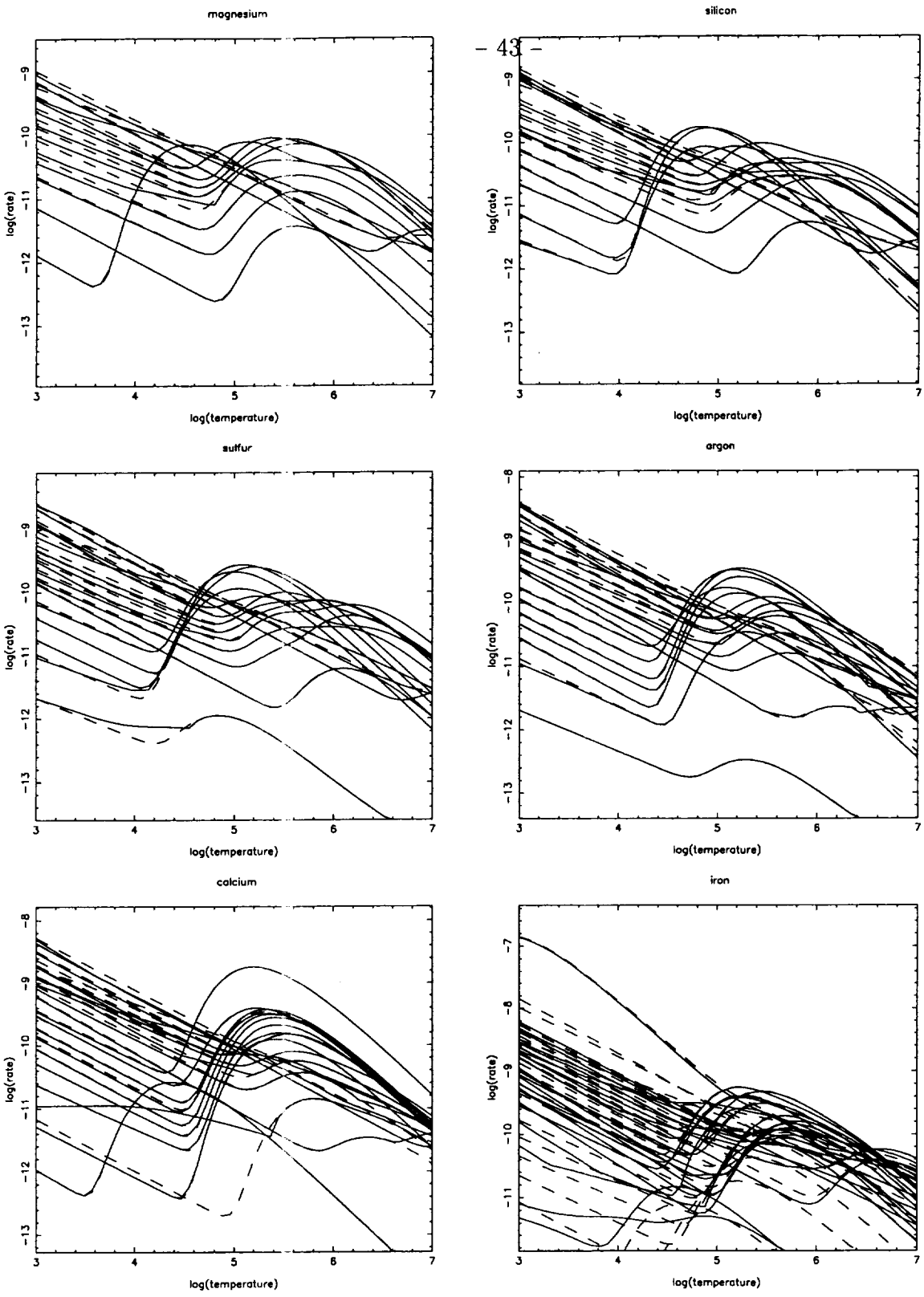
magnesium
silicon
sulfur
argon
calcium
iron
log(rate)
log(temperature)

Fig. 4.— b

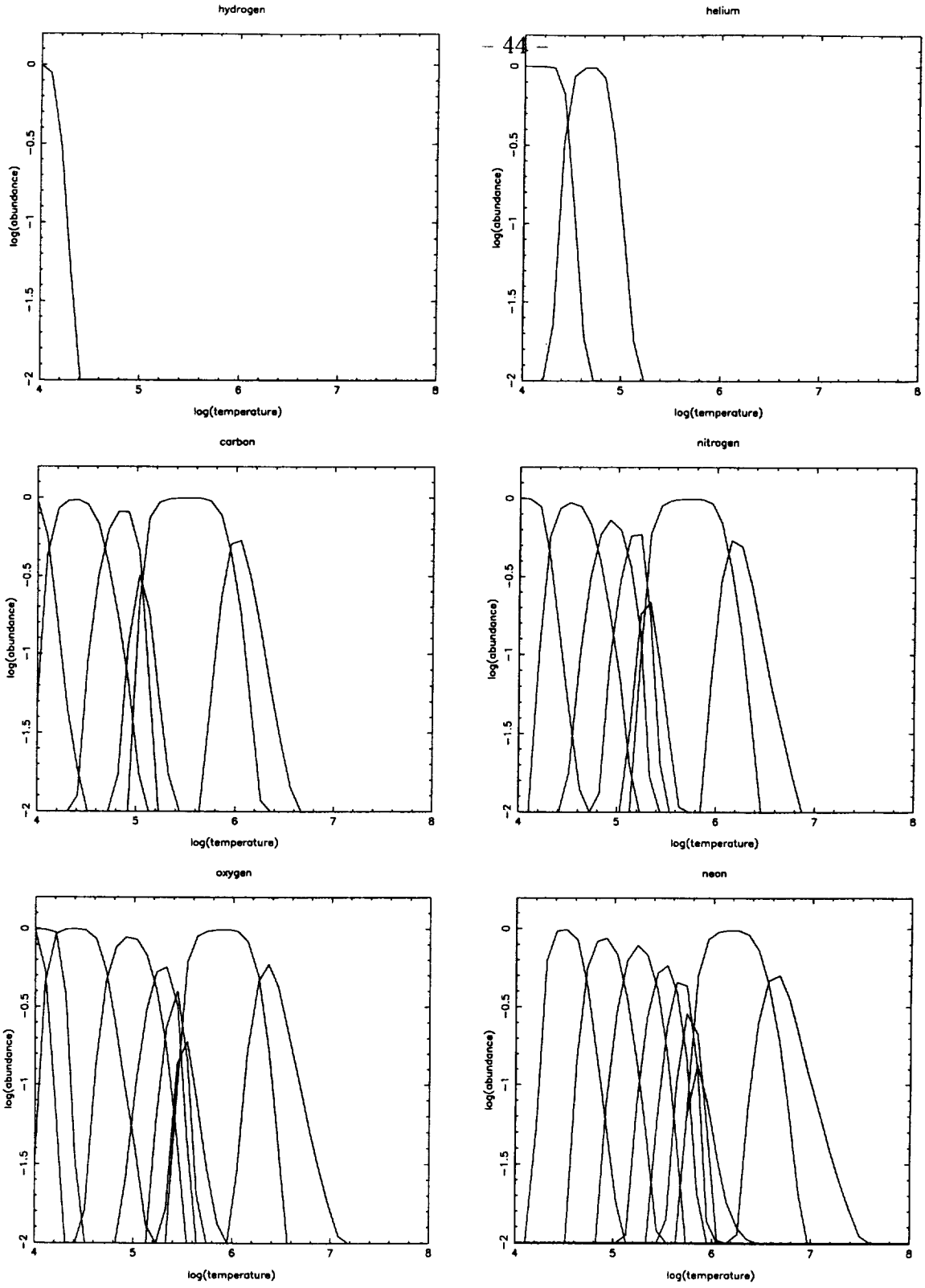
hydrogen
helium
carbon
nitrogen
oxygen
neon
log(abundance)
log(temperature)
0
−0.5
−1
−1.5
−2
4
5
6
7
8

Fig. 5.— a

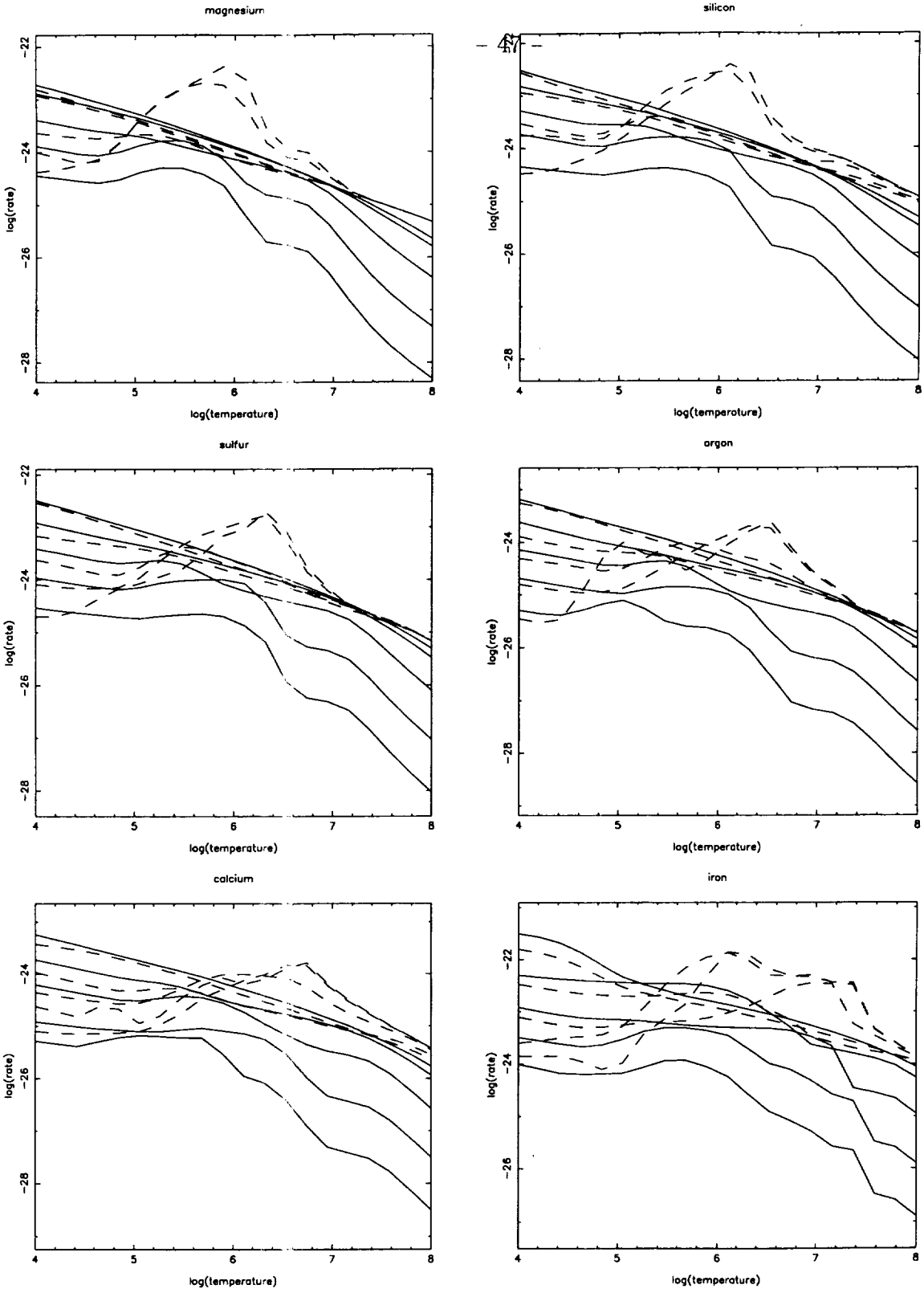
magnesium
silicon
sulfur
argon
calcium
iron
log(rate)
log(temperature)
-22
-24
-26
-28
4
5
6
7
8

Fig. 6.— b

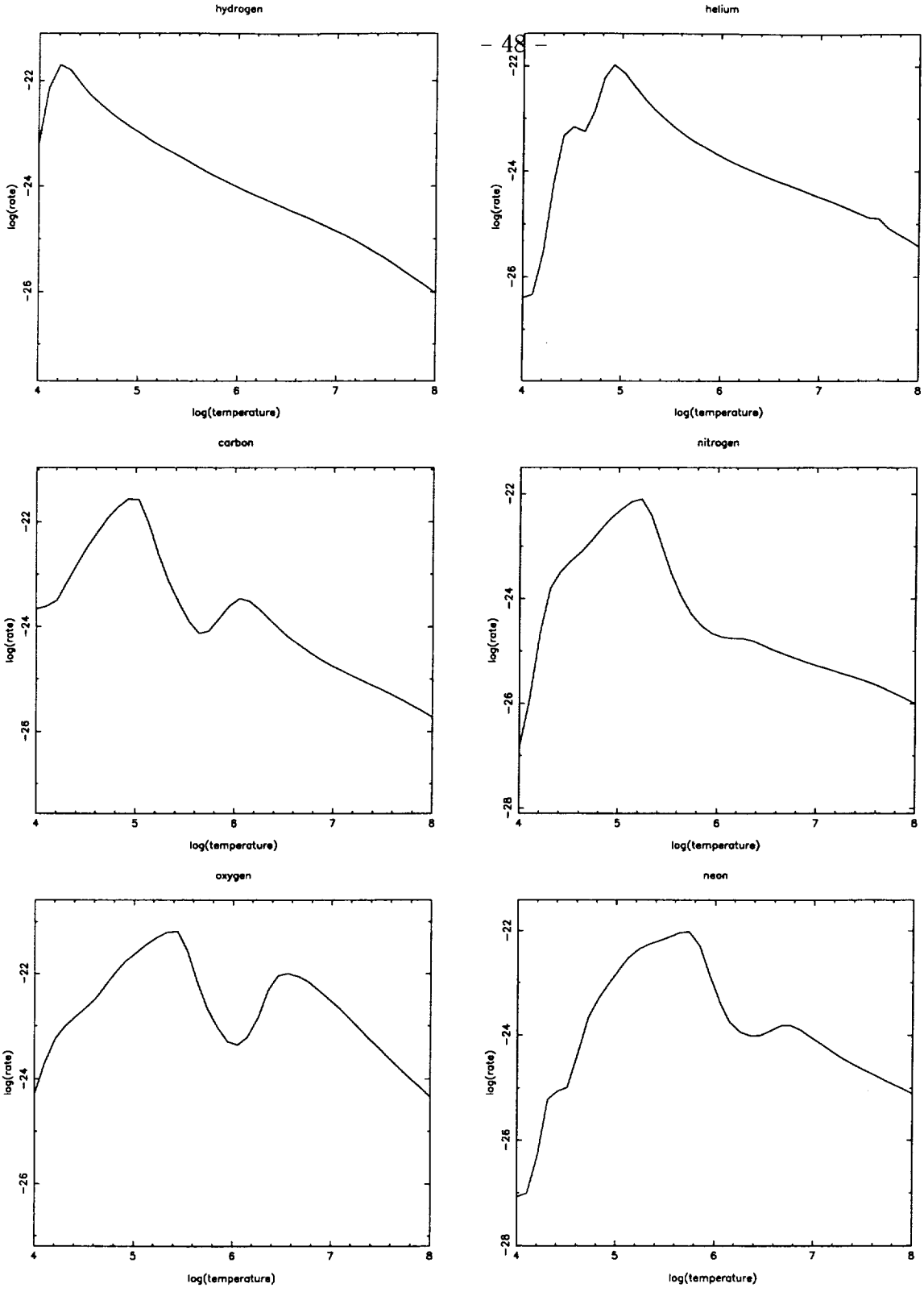
hydrogen
helium
carbon
nitrogen
oxygen
neon
log(rate)
log(temperature)

Fig. 7.— a

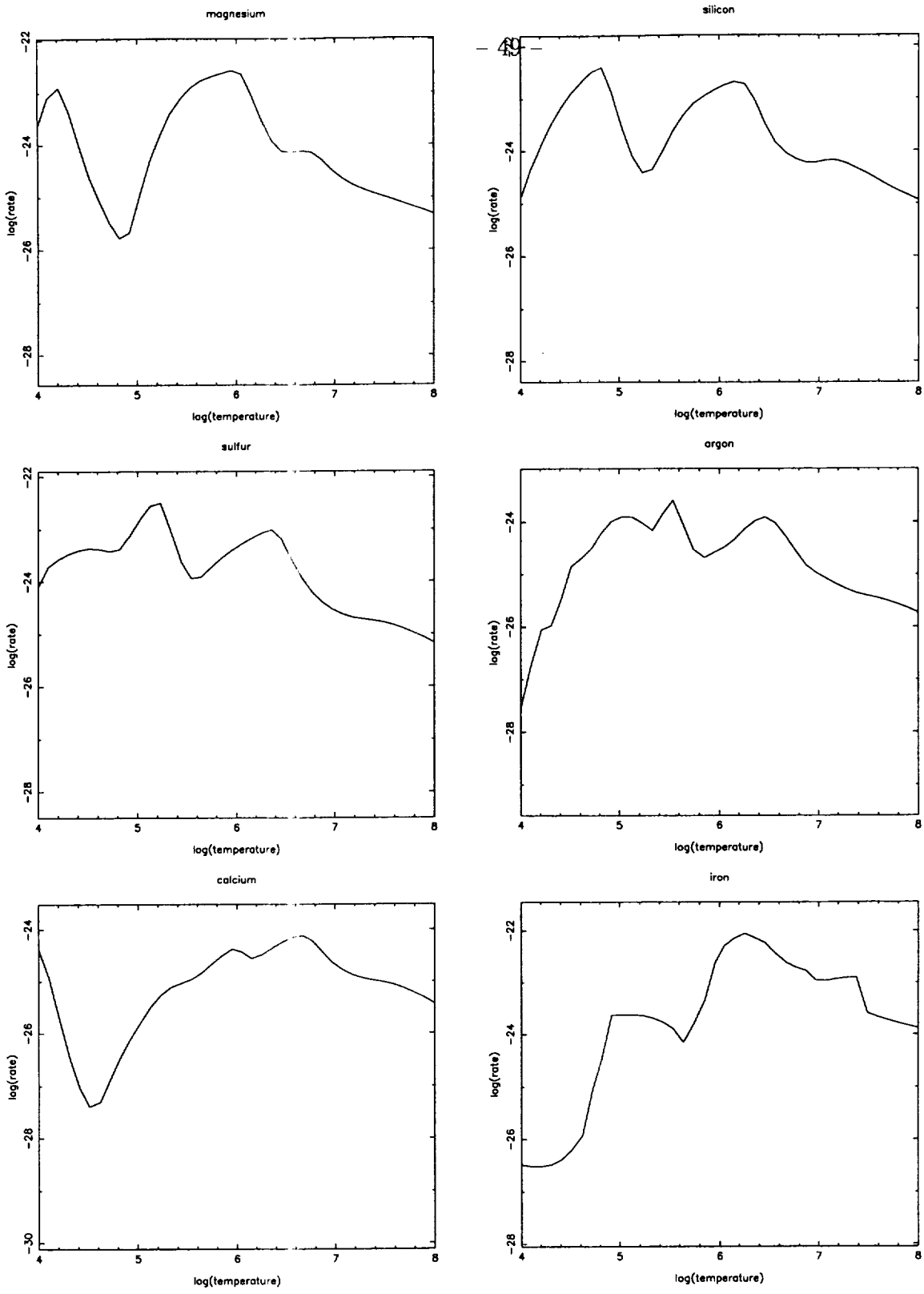
magnesium
silicon
sulfur
argon
calcium
iron
log(rate)
log(temperature)

Fig. 7.— b

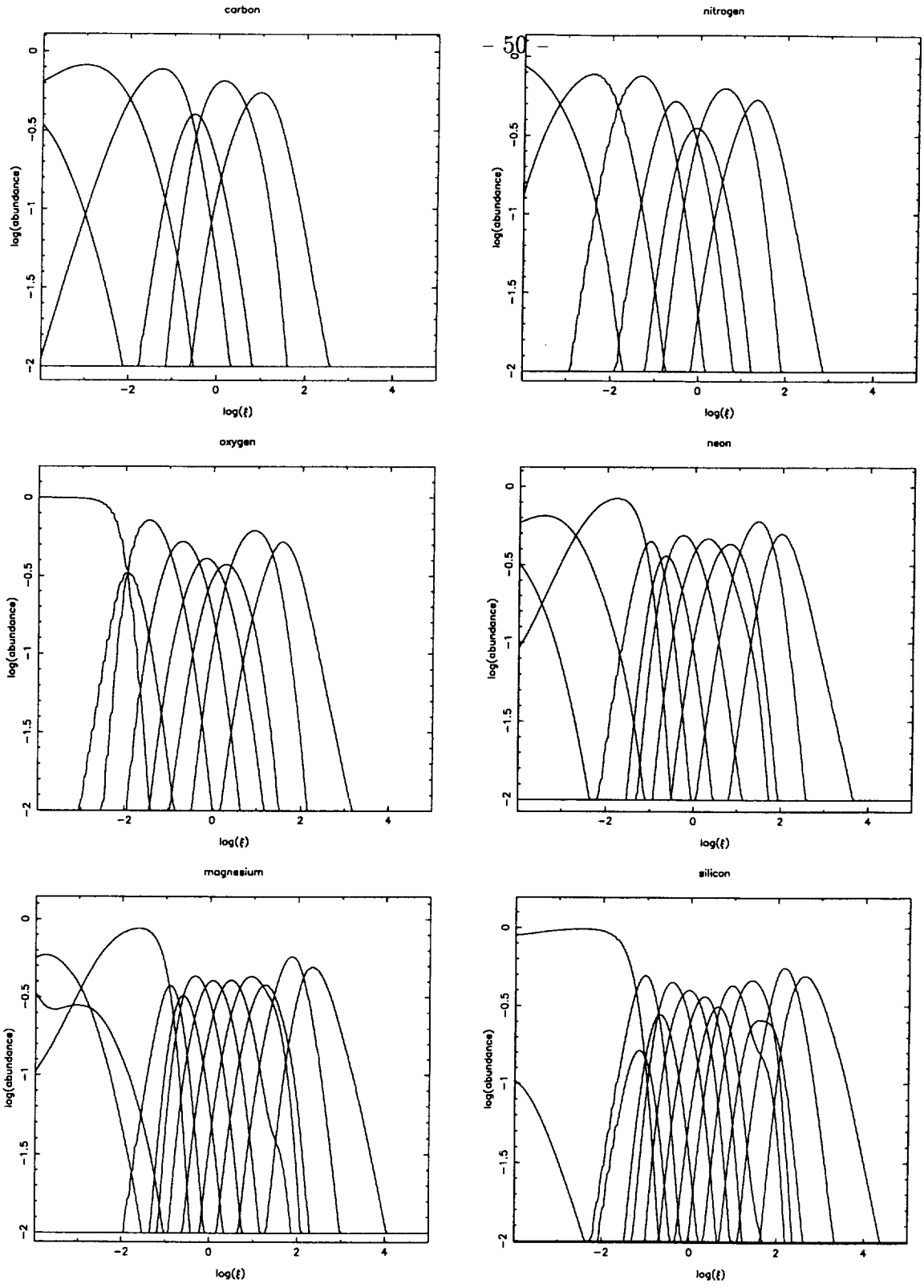
carbon
nitrogen
oxygen
neon
magnesium
silicon
log(abundance)
log(t)

Fig. 8.— a

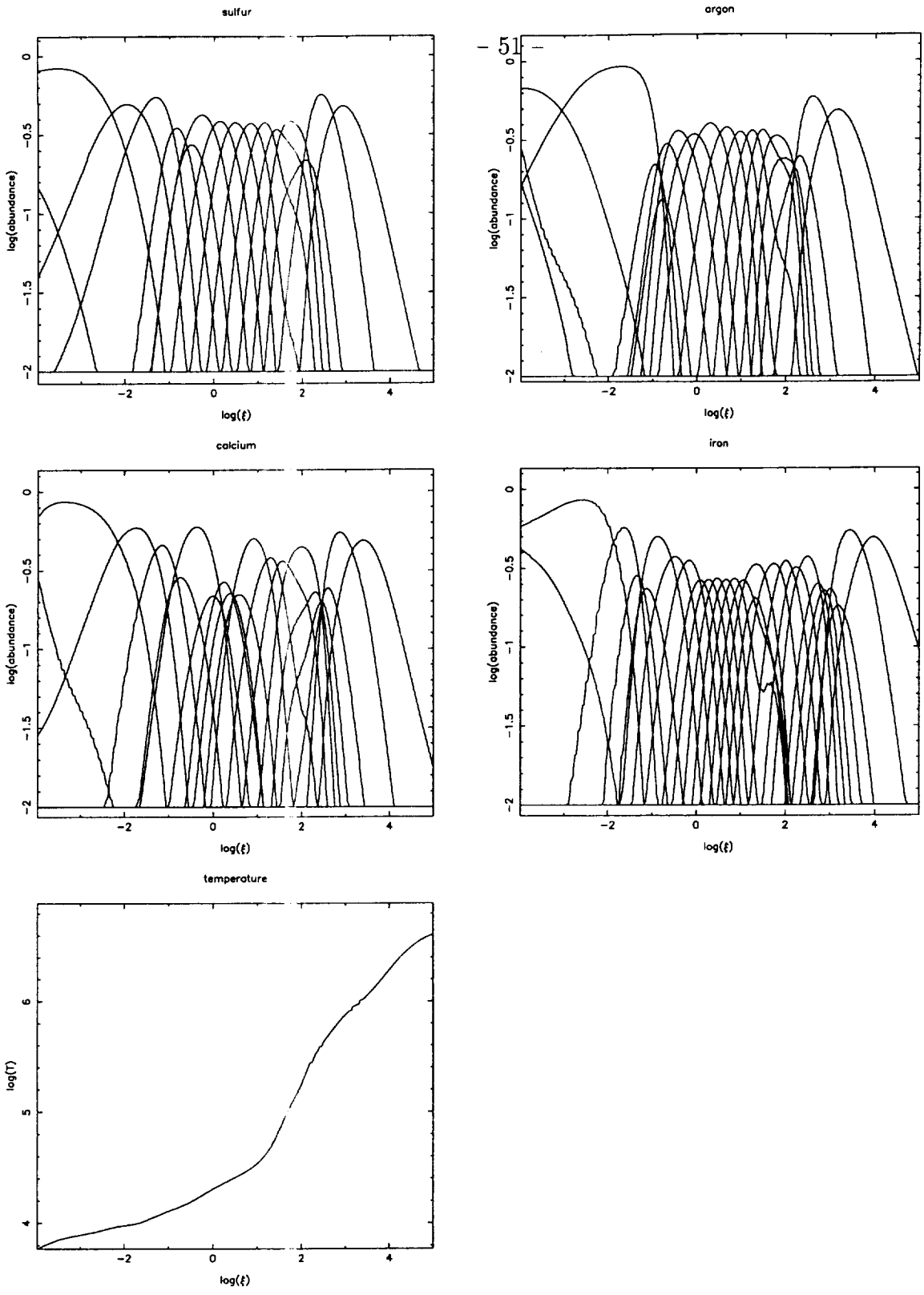
sulfur
argon
calcium
iron
temperature
log(abundance)
log(T)
log(ξ)

Fig. 8.— b

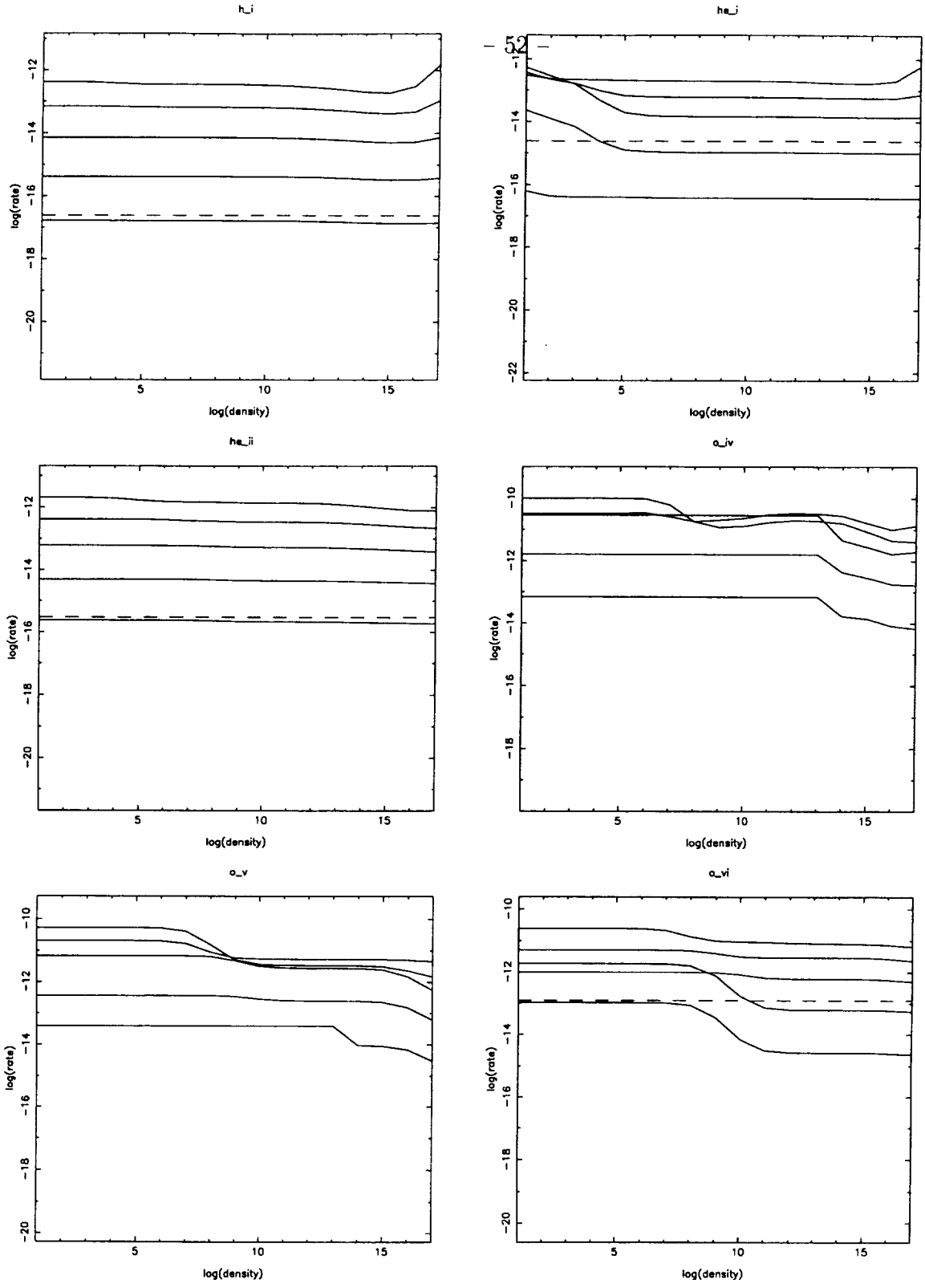

Fig. 9.— a

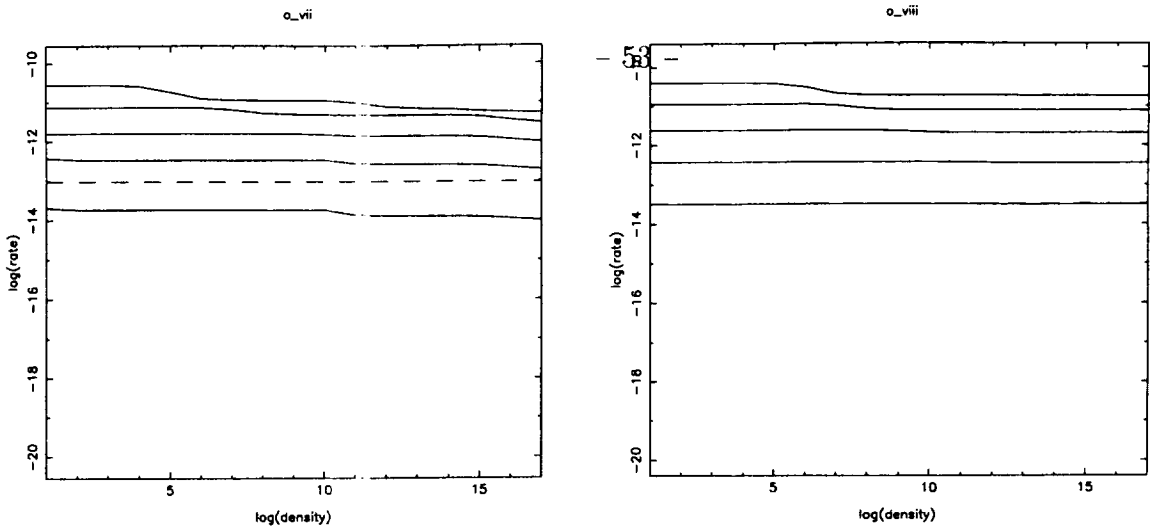

Fig. 9.— b

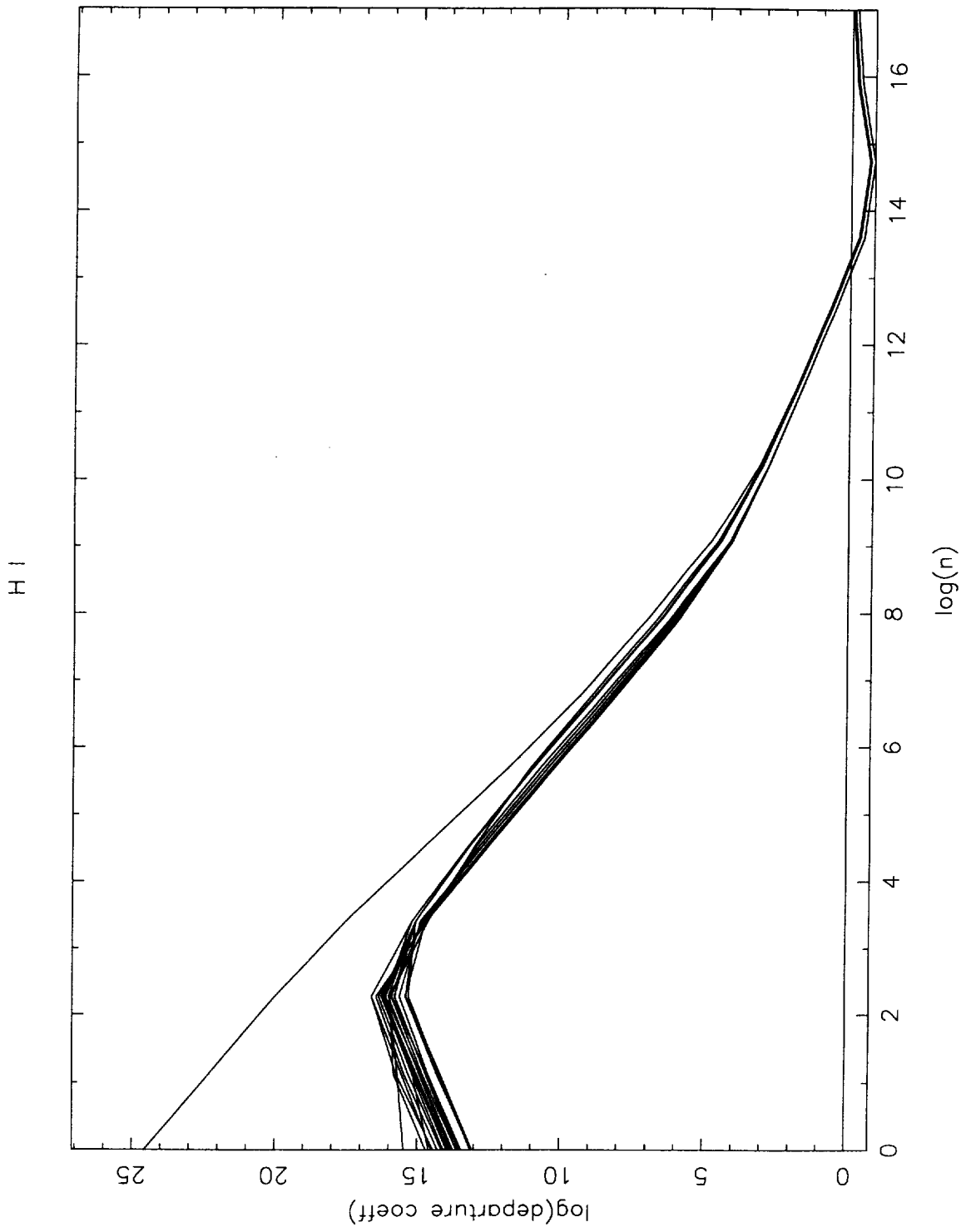

Fig. 10.— a

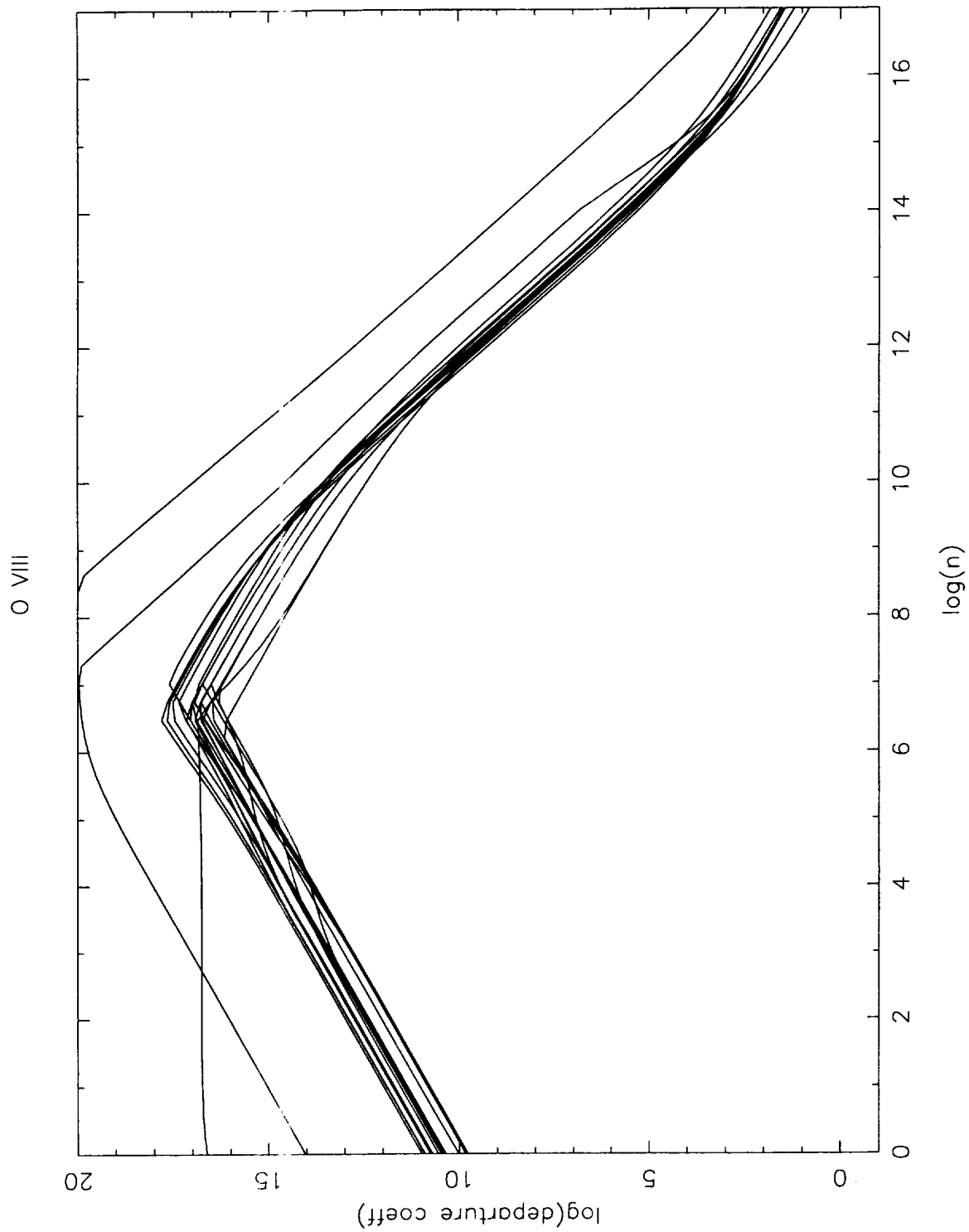

Fig. 10.— b

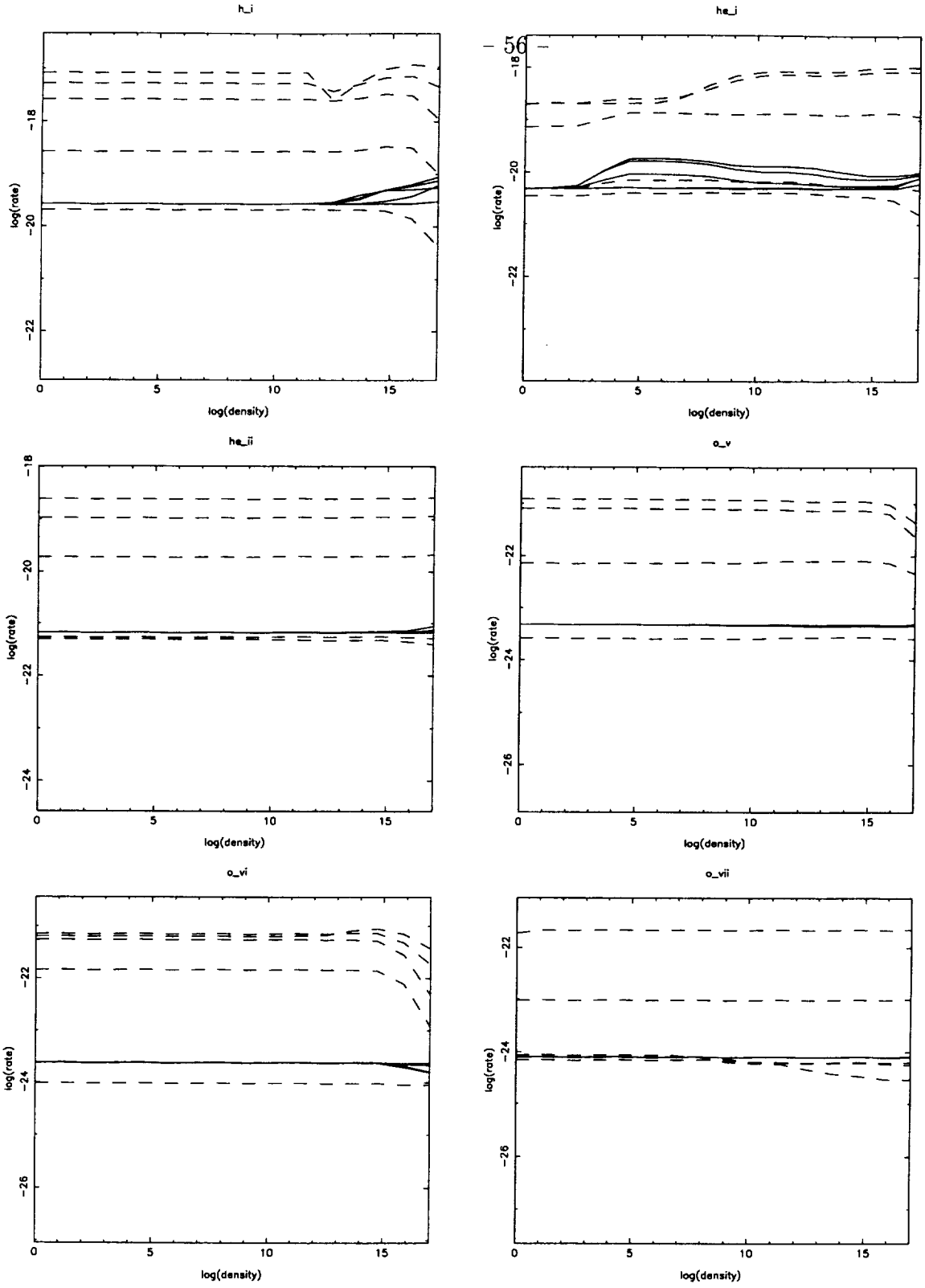

Fig. 11.— a

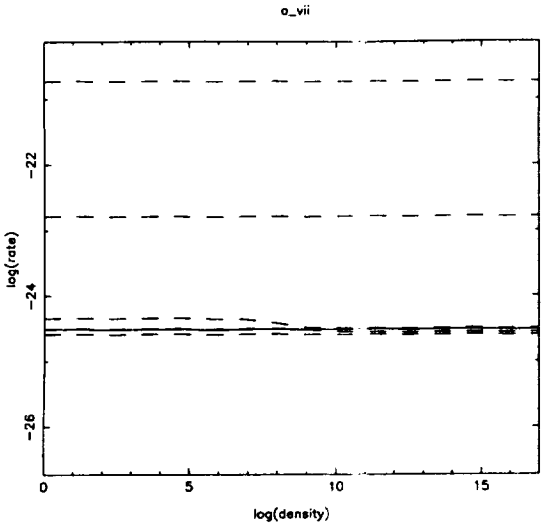

Fig. 11.— b

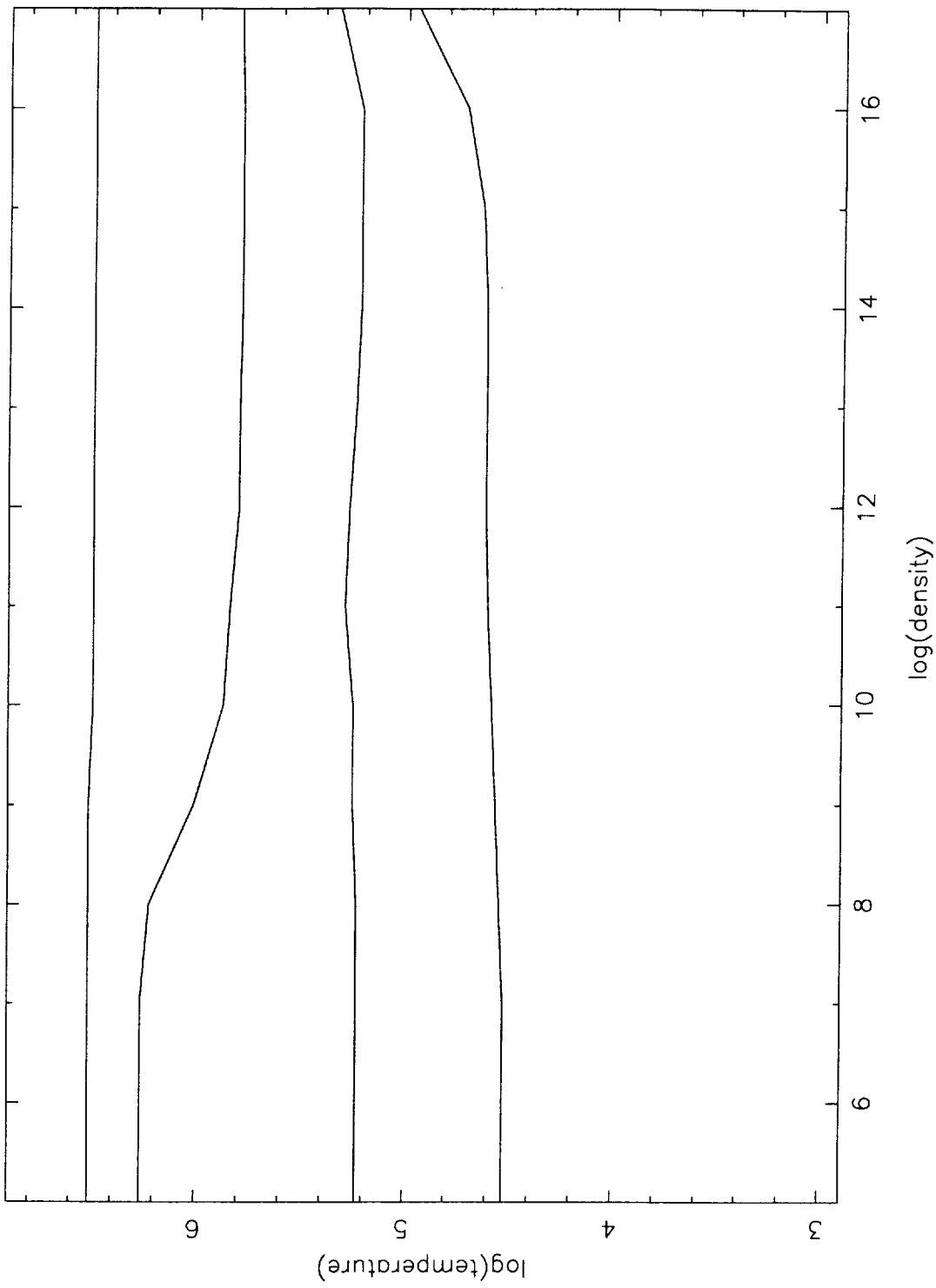

Fig. 12.—

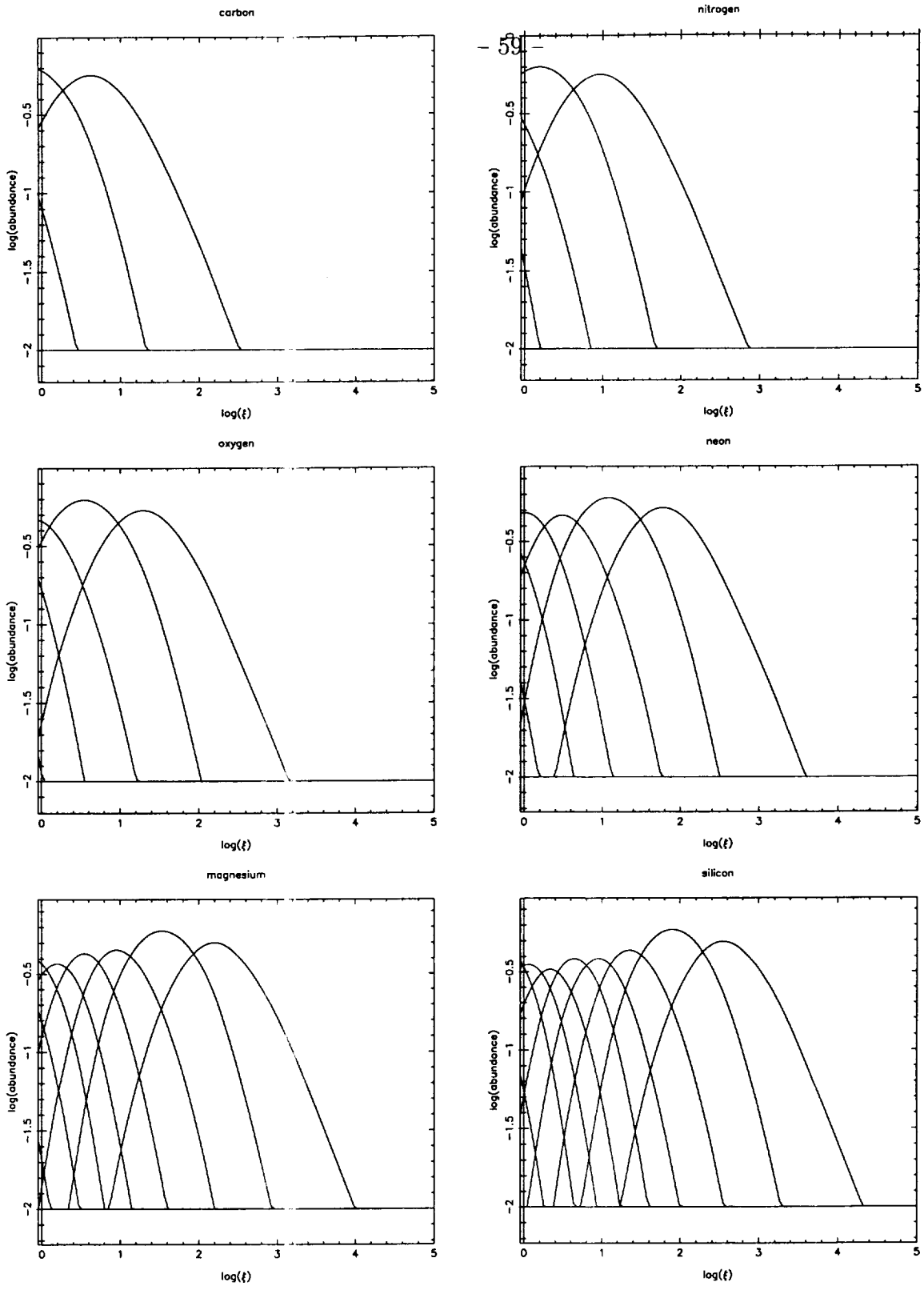
carbon
nitrogen
oxygen
neon
magnesium
silicon
log(abundance)
log(ξ)
0
1
2
3
4
5
−0.5
−1
−1.5
−2

Fig. 13.— a

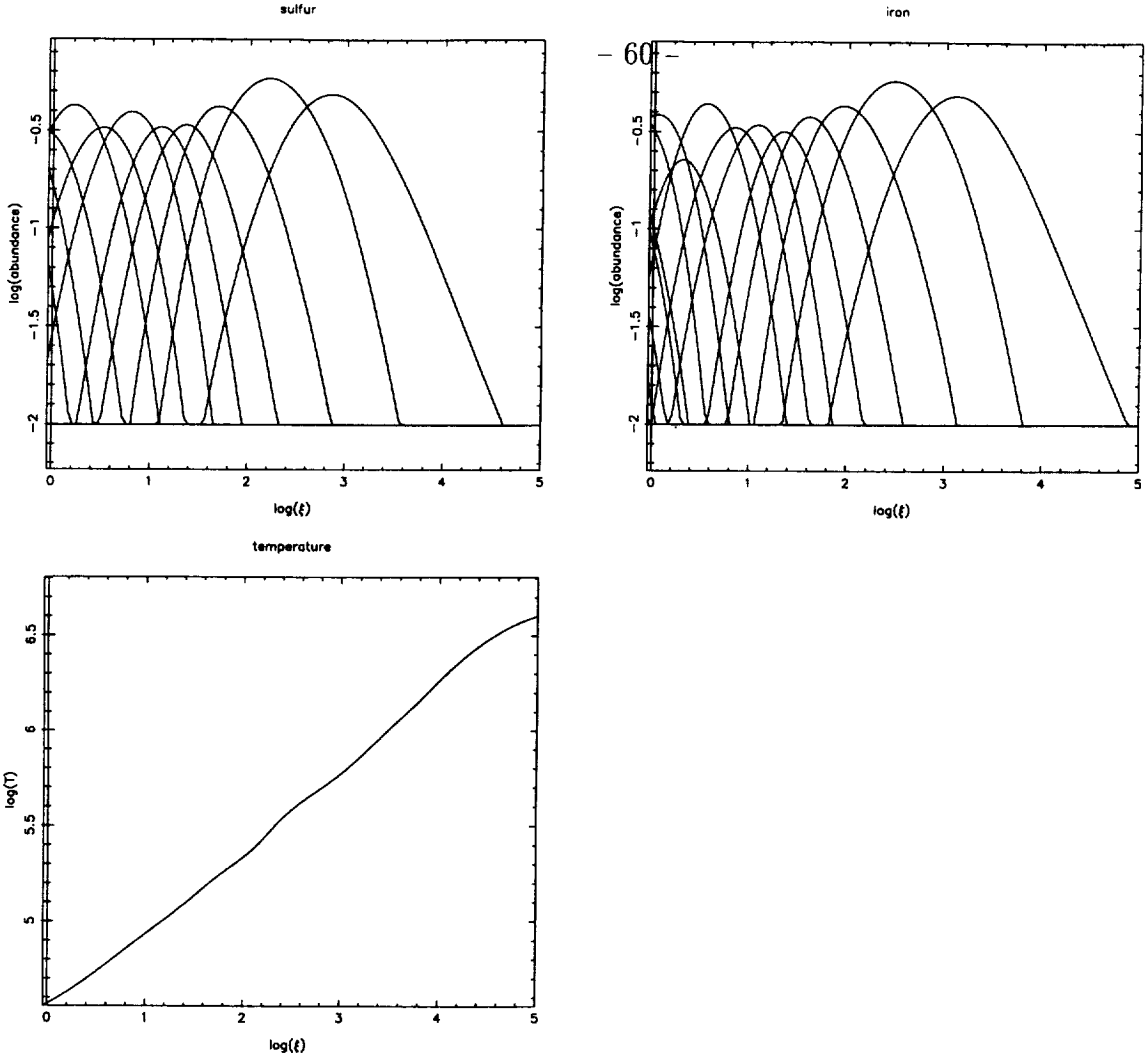
sulfur
log(abundance)
log(ℓ)
iron
log(abundance)
log(ℓ)
temperature
log(T)
log(ℓ)

Fig. 13.— b

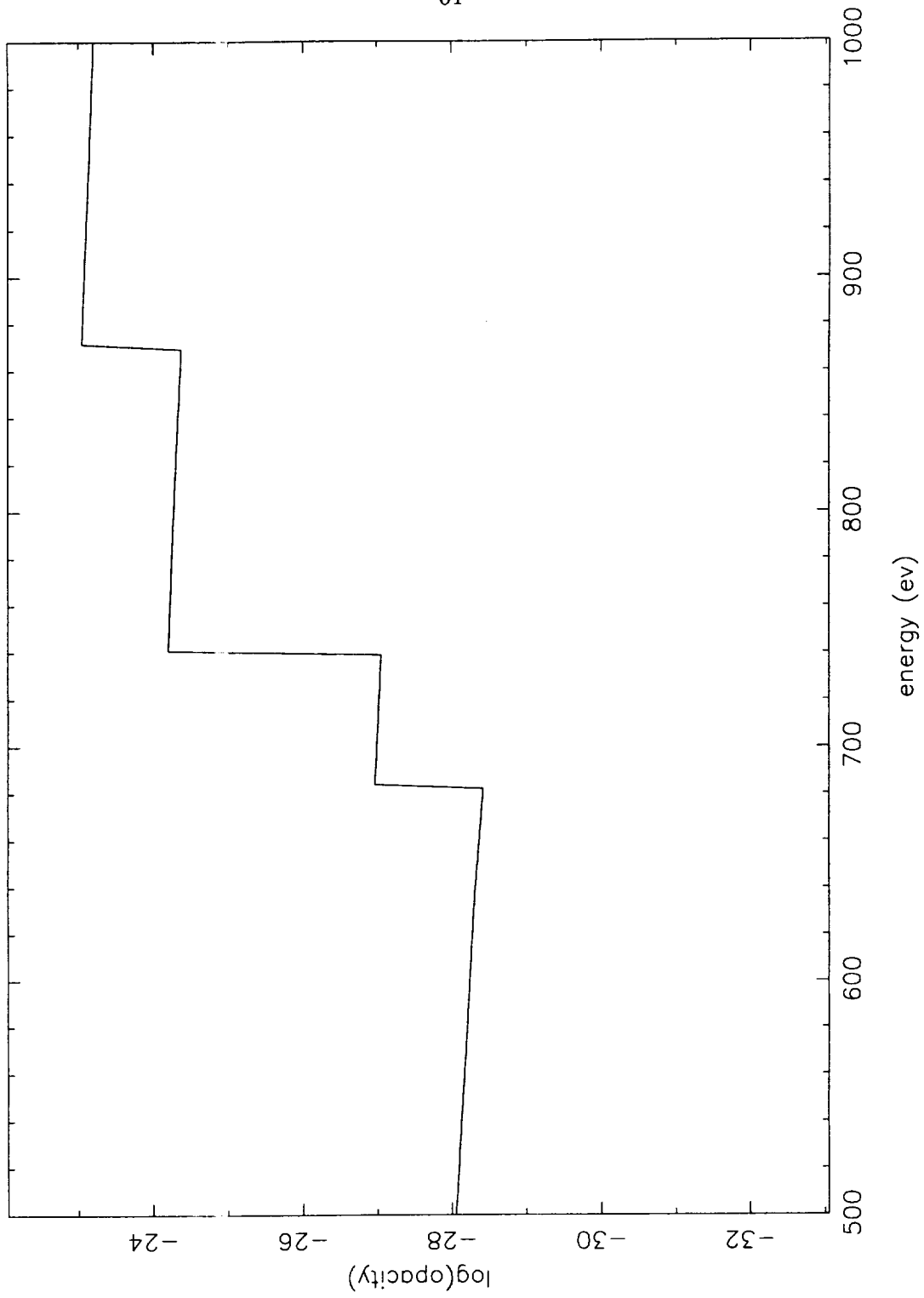

Fig. 14.— a

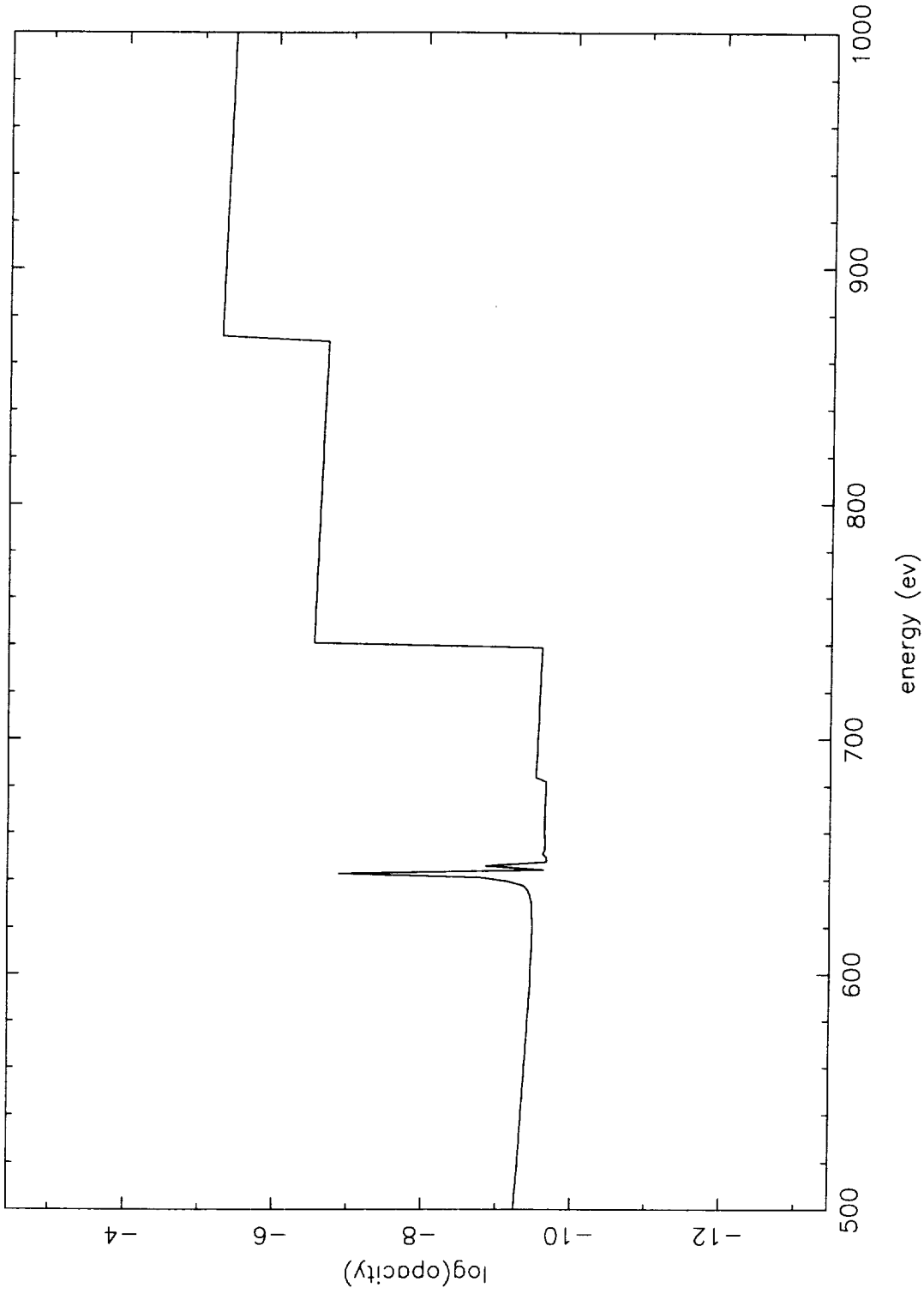

Fig. 14.— b

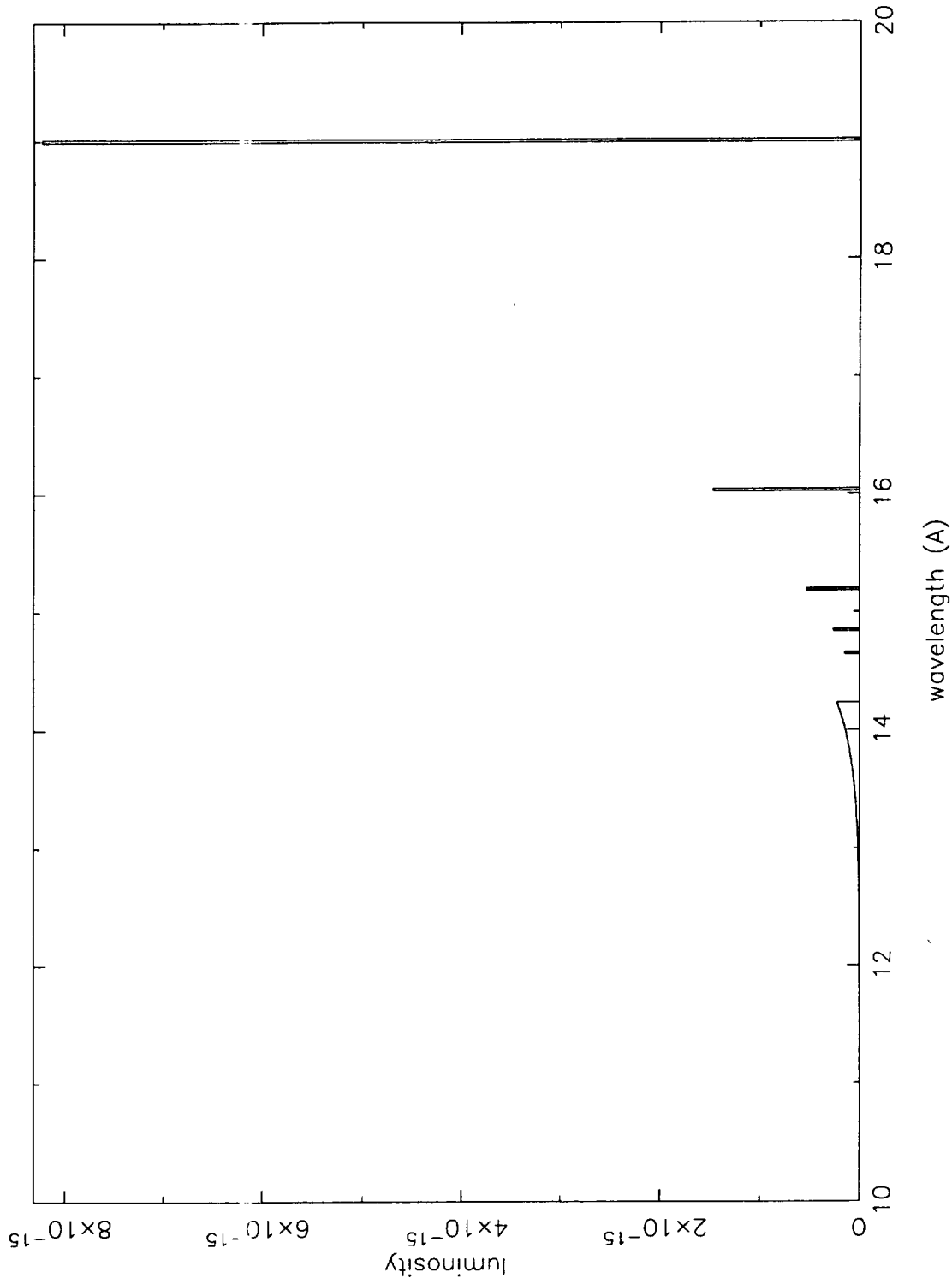
luminosity
0
2×10⁻¹⁵
4×10⁻¹⁵
6×10⁻¹⁵
8×10⁻¹⁵
wavelength (A)
10
12
14
16
18
20

Fig. 15.— a

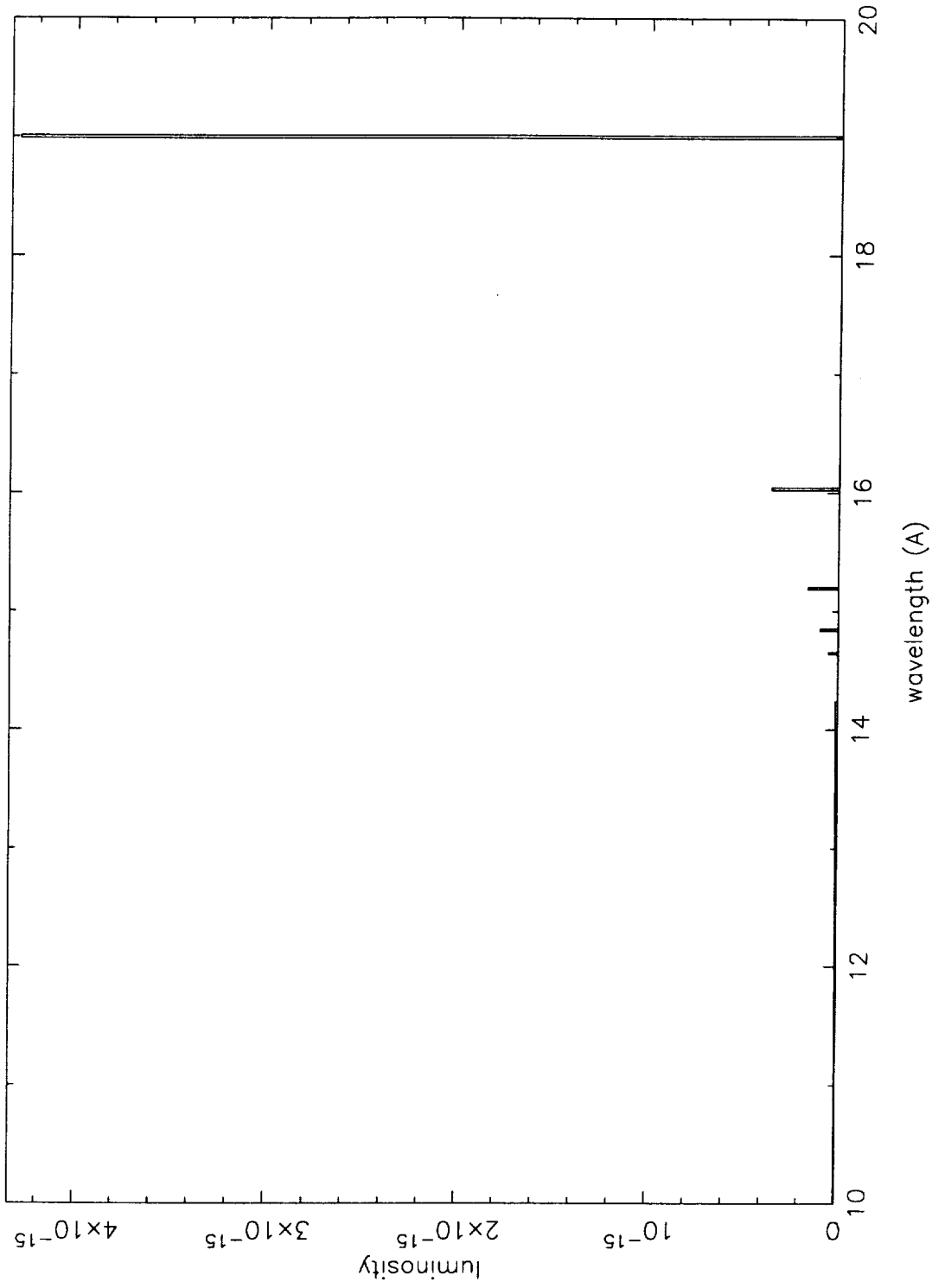
luminosity
0
10^-15
2×10^-15
3×10^-15
4×10^-15
10
12
14
16
18
20
wavelength (A)

Fig. 15.— a

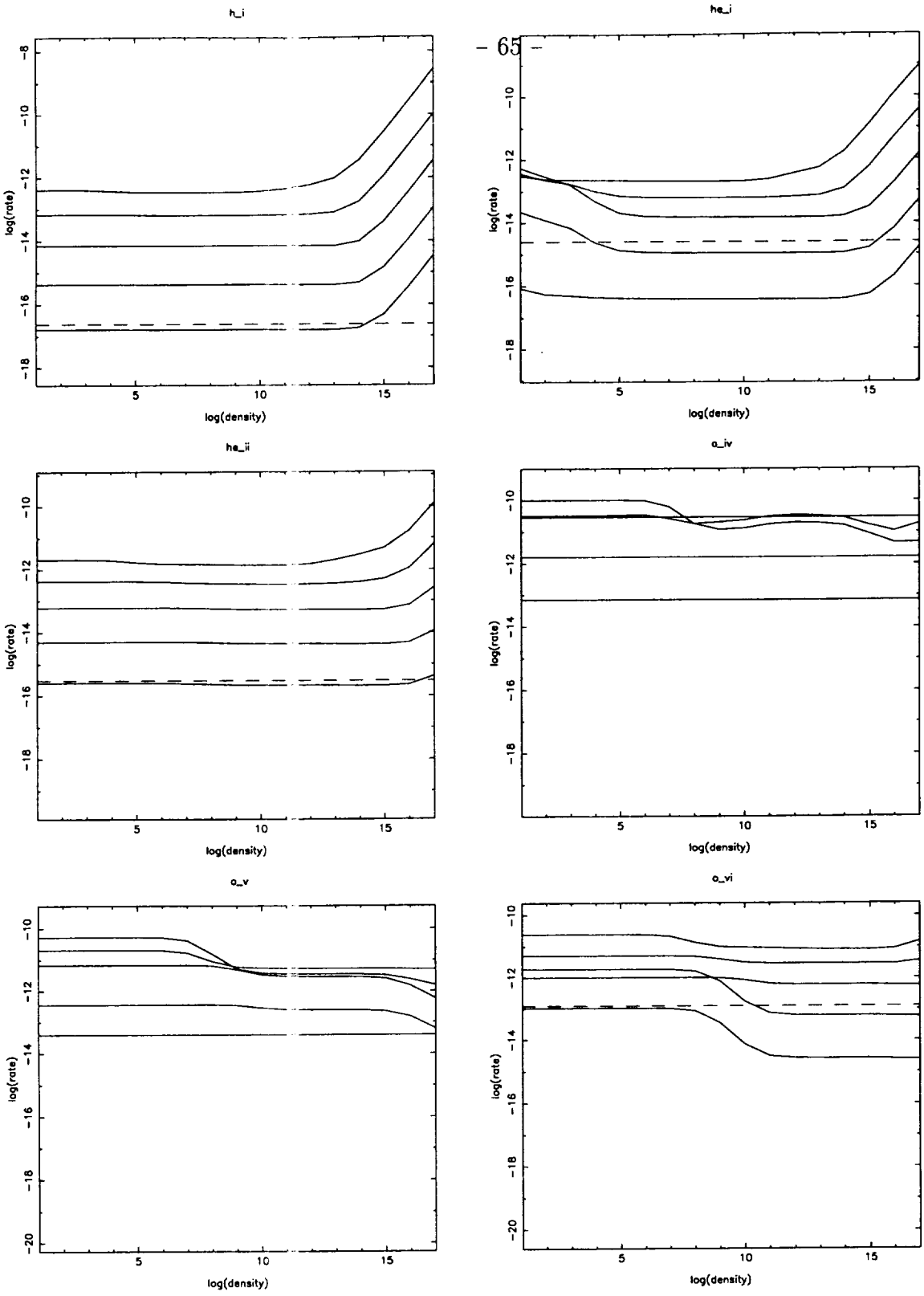

Fig. 16.— a

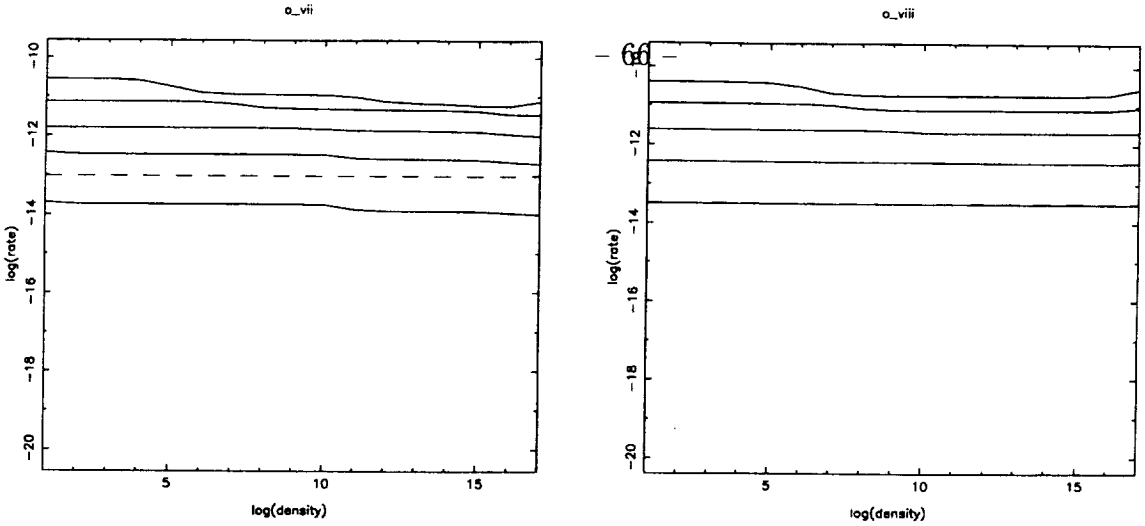

Fig. 16.— b